DOUBLE-BLIND REVIEW

Quick clay monitoring using distributed acoustic sensing: A case study from Rissa, Norway

Running head: Quick clay monitoring using DAS

Robin André Rørstadbotnen[1], Hefeng Dong[1], Martin Landrø[1], Kenneth Duffaut[2], Kevin Growe[1], Umedzhon Kakhkhorov[2], Susann Wienecke[3], Joacim Jacobsen[3]

1: Norwegian University of Science and Technology, Department of Electronic Systems, NO-7491, Trondheim, Norway

2: Norwegian University of Science and Technology, Department of Geoscience and Petroleum, NO-7491, Trondheim, Norway

3: Alcatel Submarine Networks Norway AS; Tiller, Norway

E-mails: robin.a.rorstadbonen@ntnu.no

hefeng.dong@ntnu.no ; martin.landro@ntnu.no ; kenneth.duffaut@ntnu.no ;

kevin.growe@ntnu.no ; umedzhon.kakhkhorov@ntnu.no ; susann.wienecke@asn.com ;

joacim.jacobsen@asn.com

Original paper date of submission: 25 April 2022

First revision of paper date of submission: 11 October 2022

Second revision of paper date of submission: 25 January 2023

Third revision of paper date of submission: 19 April 2023

Fourth revision (acceptance pending) of paper date of submission: 05 June 2023

Quick Clay Monitoring using Distributed Acoustic Sensing: A case study from Rissa, Norway

(June 5, 2023)

Running head: **Quick Clay Monitoring using DAS**

ABSTRACT

Quick clay avalanche is one of the most devastating landslide types worldwide. Hence, an early-warning system is in demand to mitigate fatal consequences caused by such events. To address this, distributed acoustic sensing data are collected in an area containing quick clay deposits between July 2021 and February 2022 in Rissa, Norway, while a new road is constructed on the quick clay. Road construction can induce unwanted changes to the mass balance in the clay, and previous landslides have been triggered by such changes. For this purpose, both passive and active data are collected to test and compare various analysis methods. Using extracted Rayleigh wave dispersion from active sledgehammer shots, shear-wave velocity depth profiles covering the first 15 m could be estimated and compared using a linearized and a non-linear surface wave inversion method. Furthermore, ambient noise cross-correlation is used to obtain the dispersion from the ambient noise and associated shear-wave velocity profiles, providing two possible data collection methods for the early-warning system. The obtained dispersion curves and the estimated shear-wave velocity profiles show small time-laps variation during the acquisition period (up to $\simeq$23 m/s), where the variation is within one standard deviation. Such small variation suggests that the construction work and the extra load added to the quick clay do not alter the quick clay's properties. Nevertheless, the obtained results capture the non-repeatability effects within the acquisition period and provide reference curves for the study area at undisturbed conditions and valuable information for future

comparisons to potential failure scenarios. This is the first step in exploring an early-warning system for quick clay landslides using fiber-optic cables. Further work will investigate the possibility of automatizing the system and improving the accuracy of the sensing system.

INTRODUCTION

In recent years several devastating quick clay landslides have been triggered by changes in the near-surface properties of the clay through anthropogenic and natural impacts. Different disturbances have been shown to trigger such liquefaction, e.g., vibrations from earthquakes, altering the material balance in the clay by moving cubic meters of mass, massive rainfalls over time, or erosion from a nearby drainage network (Gregersen et al., 1981; Lundström et al., 2009; Ryan and Riekeles, 2021). In Norway, Sweden, and Canada (and other countries previously covered by glaciers), the majority of the devastating landslides can be categorized as quick clay landslides (Lundström et al., 2009). There have been several quick clay slides in Norway over the last 50-60 years. Examples are the slides at Trögstad in 1967, at Rissa in 1978 (Gregersen et al., 1981), and most recently at Gjerdrum in 2020 (Ryan and Riekeles, 2021). Moreover, the shear strength of the clay will drastically decrease before such landslides and vanish when the quick clay liquefies (see NGI (2011) for a YouTube video of the Rissa landslide). The time scale for this change in shear modulus is unknown and represents a significant challenge for such monitoring projects as proposed here. As the shear-wave speed is related to the shear strength, the quick clay changes can be monitored by investigating the changes in the shear-wave speed. Therefore, developing an early-warning system for quick clay landslides is possible.

Distributed Acoustic Sensing (DAS) has been shown to be an effective and appropriate near-surface monitoring system (Dou et al., 2017). DAS can re-purpose existing ”dark” Fiber Optic (FO) cables (fibers not used for data transfer) or be part of a dedicated recording system where FO cables are installed for a specific application. Both record in-line strain in the cable down to nano strain levels. Historically, DAS has been applied to dedicated vertical fibers in downhole operations (Mestayer et al., 2011) and has only recently been applied to horizontal fibers. The DAS

recording system has several advantages compared to conventional seismic sensors; it has both a high temporal and spatial resolution, with sample rates down to meters and up to kilo-hertz. It is a low-maintenance receiver array with possibilities of short to long-range monitoring by interrogating cables stretching from 500 m (using a 100 kHz sample rate) to 150 km ($\simeq$667 Hz; Waagaard et al. (2021)). DAS technology has already been applied to many disciplines, including near-surface monitoring (Table 1), earthquake seismology (Lindsey et al., 2017), geophysical exploration (Mestayer et al., 2011; Taweesintananon et al., 2021), water-born sound sources (Matsumoto et al., 2021), and passive acoustic monitoring of ships (Rivet et al., 2021) and baleen whales (Landrø et al., 2022; Bouffaut et al., 2022).

Currently, it is common to have more optical fibers than required for the installation of telecommunication cables, as it incurs minimal additional cost and adds redundancy. In terms of telecommunications applications, these additional fibers are typically left unused ("dark") and can therefore be exploited for other applications, such as DAS. Alternatively, fiber cables can be installed as part of dedicated recording systems for a specific application, like in this study. The DAS interrogator (OptoDAS) used in this work repeatedly sends linear frequency-modulated pulses into the fiber and interrogates the Rayleigh backscattering caused by density fluctuations in the fiber (Waagaard et al., 2021). These density fluctuations are displaced when, for instance, a seismic wave impinges upon the fiber. Such displacements can be detected as phase changes in the backscattered light. The time-differentiated phase is obtained by continuously comparing the backscattered response from one pulse to the next. This is done by differentiating the phase spatially between regularly spaced sections (channels) along the fiber in the backscatter response for each pulse separately and subsequently comparing it to the backscatter response from the next pulse. The number of channels over which the phase differentiation is performed is called the Gauge Length (GL). The effect of a longer GL is an improved signal-to-noise ratio (S/N) observed through stronger arrivals at higher

velocities but at the cost of attenuating shorter wavelengths. Additionally, the time-differentiation is done continuously, at a rate no faster than the time between when the pulse is sent into the fiber and the time at which the backscatter from the end of the fiber has propagated back to the interrogator, constituting the maximal temporal resolution in the DAS-data. The time-differentiated phase is stored by the interrogator and is linearly related to the fiber strain. See Hartog (2017) for more information on the conversion.

Previously, there have been several studies on near-surface changes using DAS and other seismic receiver systems. Dou et al. (2017) used two perpendicular DAS segments to image the changes in the shear-wave velocity profile in the near-surface using three weeks of traffic noise. Rodríguez Tribaldos and Ajo-Franklin (2021) analyzed five months of ambient noise to monitor seismic velocity variation caused by groundwater changes in Sacramento Valley, US. Shragge et al. (2021) did a case study for on-land DAS in Perth, Australia, using low-frequency signals to show the potential of using DAS for large-scale geophysical and geotechnical analysis finding shear-wave profiles more than 500 m into the subsurface. Furthermore, Cheng et al. (2021) used offshore fiber cables and ambient noise interferometry from Scholte waves to create 2D shear-wave velocity images of the near-surface shear-wave velocity in marine sediments, thereby improving constraints on submarine features. Olafsdottir et al. (2018) carried out a Multichannel Analysis of Surface Waves (MASW) using different geophone setups to find array configurations that increase the dispersion images' frequency bandwidth. Long et al. (2020) used hydrophone streamers and MASW on two data-sets from Ireland to find offshore shear-wave velocities from Scholte wave recordings. See Table 1 for a comparison of the content in this paper to other publications.

This paper aims to show how surface waves recorded on dedicated FO cables can be used as part of a monitoring procedure to map the changes in quick clay attributes with time, such as the shear stiffness and velocity, as a new highway is built on the clay. The area under investigation consists of

a 3-6 m sediment layer (including a 0.5-1 m top layer of soil), followed by a 15 m thick marine clay and quick clay layer overlaying glacial marine deposits (Solberg et al., 2012). The new road will introduce changes in the mass load of the clay and can potentially induce unwanted alterations to the quick clay properties. To address this, two different data-sets are collected over seven months using a dedicated FO array trenched in a known quick clay area: (1) using an active seismic source, a sledgehammer on a steel plate; (2) using different ambient noise sources, both directional industrial noise generated by the highway construction and isotropic ambient noise from quiet evenings and weekends. We use a subset of this passive data-set to prove the feasibility of using passive seismic interferometry in such a monitoring system. Furthermore, to find the variation in the quick clay layer, dispersion curves obtained from the data-sets are used as input to two different inversion algorithms, one linear and one non-linear. These are compared to find the procedure best suited for the monitoring system and to find potential alterations in shear-wave velocity over the seven months period.

The paper is organized into four parts: The first part describes the data acquisition and data analysis. In the second, the surface wave inversion algorithms are briefly presented. The third part presents and discusses the results. Results from the active data and the background noise from quiet periods are presented and compared in the main text, while results using the construction noise are presented in supplemental materials. Finally, the conclusions are made.

DATA ACQUISITION AND ANALYSIS

DAS data acquisition

In order to investigate different monitoring procedures for quick clay avalanches using FO cables, time-differentiated phase data recorded by the OptoDAS interrogator are acquired in Rissa, Norway

(see Figure 1). The acquisition started in July 2021 and lasted until February 2022, recording data using four 2.02 km long FO cables spliced together, providing a total cable length of 8.08 km. The cable layout is depicted in Figure 1C. The laser sweep is sent through the interrogator unit into the first cable and propagates South into well 1 (W1) and subsequently into well 2 (W2). When exiting well 2, it turns north and travels on the same path until it reaches the northernmost yellow cross in Figure 1C, then it travels to the base, entering the next cable. The configuration path is repeated four times. Data recorded on the first round (on a Corning loose tube cable) are studied in this work. The cables are trenched at a maximum depth of 40 cm into the subsurface.

Both active and passive data are acquired. A total of $\simeq$2340 sledgehammer shots are recorded for the active data, with passive data recorded at intermittent intervals for the whole seven month period (with small breaks due to power outages). However, only $\simeq$300 shots at roughly 0.5 m distance from well 1 have been analyzed, as well as 28 shots on the northern segment (see the yellow asterisk and the highlighted sections in Figure 1C at the 1469 & 1752 m marks). In addition, a follow up survey was carried out on 2022.03.22 to investigate the effect of varying the GL during acquisition (for the analysis of the various GL, see Appendix A). The acquisition parameters are listed in Table 2. Figure 2 depicts examples of the recorded data, from both the active and passive periods, at a distance of 100-700 m along the cable from the interrogator to get an overview of the typical signals present during the acquisition period. This study mainly focuses on data recorded on a 168 m section of the Corning loose tube cable inside an area containing quick clay. The segment starts when the cable exits well 1 at a distance of 413 m (where the corresponding trace is used as trace 0 in the following analyses), ending when entering well 2 at 581 m (as indicated by the orange segment in Figure 1C). This segment is conveniently placed, as it is easy to define its start and end points due to the clear presence of wells 1 and 2 in the data (see, e.g., Figure 2A, C). The wells are observed as two low amplitude regions at distances 363-402 m and 582-695 m, respectively (cable

in well 2 goes up and down twice). They are drilled 19 m into the quick clay to facilitate additional studies and provide information on subsurface properties, such as water table level and bedrock depth. Only information from the drilling itself has been used here; the DAS data in the wells are outside the scope of this work.

The active data are acquired using sledgehammer shots on a steel plate. Figure 2A displays example shots from 2021.08.12. Different types of shots at the same shot position are carried out for each acquisition date: vertical blows (P-shots), horizontal in-line with the array (S-shots, Hx), and horizontal cross-line with the array (S-shots, Hy). In practice, the P-shots are executed by the sledgehammer hitting the top of the steel plate. In contrast, for the S-shots, the sledgehammer strikes the vertical sides of the steel plates, parallel with the array for in-line shots and perpendicular to it for cross-line shots. Figure 3A depicts one of the P-shots by well 1 from the acquisition in August 2021, and clear dispersive Rayleigh waves can be observed. The dispersive data inside the black box indicated in Figure 3A are used to compute the dispersion image shown in Figure 3B, where the data outside the black box are muted. The dispersive behavior of the Rayleigh wave is also clear in the obtained dispersive image, and several higher-order modes are present. Furthermore, the different sledgehammer strikes are compared to find which shot type provided the best dispersion image (see supplemental Figure S1). Data recorded for the in-line S-shots showed the most energy, followed by the P-shots and the cross-line S-shots, consistent with radiation patterns in Kähler and Meissner (1983). However, only the P-shots produced clear Rayleigh wave modes, while the in- and cross-line S-shots generated a mix between Rayleigh and Love waves. Thus, the P-shots are used to obtain the best Rayleigh wave dispersion image in this analysis and are recommended for surface wave analysis similar to the one presented here. Moreover, the most predominant noise generated during the data acquisition came from road construction, through trucks and excavators. Due to these, some of the shots are masked by noise and unusable for analysis. Even at distances up to

500 m, the construction work rendered shots useless. However, this could easily be circumvented by carrying out the shots during breaks in work or outside working hours.

Figures 2B-C shows two examples of one-hour ambient noise used for the seismic interferometry to extract Virtual Shot Gathers (VSG). The first segment is acquired during a weekend (2021.08.14), and the second during a weekday at the start of the road construction (2021.08.18). Different events are clearly visible in the data. The noise recorded during the weekend in Figure 2B is evenly distributed with low amplitude, while the industrial noise in Figure 2C shows high amplitudes when road construction is ongoing. The site for acquiring data is, normally, a quiet area, as observed in Figure 2B. Only a farmhouse is located close to the buried cables. In addition, a road is located 150-300 m from the cable, and only a few cars pass even during workdays. Passive data is acquired over time to investigate the possibility of monitoring changes in the quick clay. Moreover, the passive data are acquired during quiet periods and construction work. Quiet periods are here defined as periods with no construction work. Weekends are chosen as the quiet periods to analyze as they provide the longest window with isotropic noise sources uninterrupted by construction work. This work focuses on three separate weekends for three consecutive months after the road work started (2021.08.13-15, 2021.09.17-20, 2021.10.08-10). Additionally, different periods of road construction are studied to see how the position of the roadwork, relative to the segment of interest, affects the interferometry results. Two instances are studied and presented in supplemental material: (1) When the road construction started by the barn where the interrogator unit is installed (2021.08.18), 200 m from the studied segment slightly broadside, (2) when the construction is broadside to the segment (2021.09.22).

Data analysis

Phase Velocity Spectrum

The data are displayed in the phase velocity domain, also known as dispersion images, for easier identification of the different modes present in the recorded surface waves. Such images can be obtained from different methods. In this work, a $\tau - p$ transform (Verschuur, 2013) is used (see supplemental Figure S2). After computing the slant-stack, the ray parameter is inverted, and a Fourier transform along the time-axis is applied to get the phase velocity spectrum ($v_{phase} - f$).

Surface Waves from Active Source

In order to display the active sledgehammer shots, some simple pre-processing steps are carried out. (1) Data are converted from time-differentiated phase to fiber strain. (2) The mean and linear trends are removed from the data. (3) A Tukey window is applied, and the data are band-pass filtered using cut-off frequencies of 2 and 40 Hz.

In general, 40-50 shots are executed in each series for vertical and in/cross-line horizontal shots. All shots generate surface waves and show clear dispersive arrivals when not masked by the construction noise. A window including dispersive arrivals is chosen to capture the dispersion as depicted in Figure 3. The data inside the window are then transformed into the phase velocity spectrum to extract the different phase velocities used to estimate the shear-wave velocity depth profiles ($v_s(z)$).

Surface Waves from Ambient Noise Interferometry

Several steps are needed to obtain high-quality VSG, or Green's functions, from the ambient noise interferometry. The first three steps are similar to the active acquisition: (1) data are converted from time-differentiated phase to fiber strain, (2) the mean and linear trends are removed, and (3) the data are tapered by a Tukey window and high-pass filtered with a cut-off frequency of 1 Hz. In addition, (4) spectral whitening is applied by inversely weighting the complex spectrum with a smoothed version of the amplitude spectrum to produce a whitened version of the complex spectrum. This step is meant to broaden the band of the ambient noise signal used in the cross-correlation and decrease the influence of single-frequency sources (Bensen et al., 2007). Finally, (5) temporal normalization is applied to reduce the effect of transient signals in the data, like earthquakes and instrument irregularities. This work tests both 1-bit normalization and Running-Absolute-Mean-Normalization (RAMN). Both show similar results for the ambient noise, so the more adaptable and flexible RAMN method is chosen. A running window of 25 samples is used to compute the RAMN based on half the maximum period of the pass-band criteria introduced by Bensen et al. (2007).

Passive seismic interferometry using noise cross-correlations is applied to estimate the VSG and the Rayleigh wave dispersion. The channel on the segment investigated closest to well 1 ($\simeq$413 m along the cable) is chosen as the virtual source. The ambient noise recorded on the virtual source is cross-correlated with the segment's subsequent channels to generate the common VSGs. Shot gathers for 3 s time slices in a 60 min window are computed and stacked to extract the Green's functions. To enhance the coherent arrivals and increase the S/N ratio of the data, a Phase-Weighted Stack (PWS) is applied (Schimmel and Paulssen, 1997; Dou et al., 2017). From the VSG, it is possible to pick the dispersion curves in the waveform data. The left and right-hand sides of the

time-lags are averaged, and the dispersive area is selected as in the active source example and similarly transformed into the phase velocity spectrum. For the weekends, i.e., the quiet periods, the mean stack is first computed for one-hour segments. The PWS is then applied to the minimum amount of mean hourly stacks needed to enhance the surface waves in the VSG. The DAS data from August had a lower noise level than, for example, September and needed a 22-hours stack compared to the 26-hour stack for September to converge to a stable VSG (see supplemental Figure S3A). In contrast, the October stack required 30 hours (one possible explanation might be variations in weather conditions on the three dates, see supplemental Figure S4).

Figure 4 displays the VSG from the seismic interferometry for ambient noise from a quiet weekend (2021.08.14, column one) compared to an active shot recording (2021.08.12, column two). Note that the VSG has been band-pass filtered between 2 and 40 Hz to have a comparable bandwidth to the active shots. The ambient noise from the weekend is isotropic, seen through the symmetry in the retrieved Green's functions, producing well resolved Rayleigh modes (see Figure 4D and supplemental Figure S5E, F). Note that the dispersion images are normalized independently at each frequency (the normalization is similar to spectral whitening, highlighting a broader frequency range). Moreover, there are two noticeable differences between the dispersion curves from the active and ambient noise data: (1) active data contain higher frequencies than the ambient noise data; (2) the active shots hold more energy and provide higher-order modes. The latter effect can be observed in Figure 2 and Figure 4.

SURFACE WAVE INVERSION METHODS

The dispersion relations obtained from the active shots and the ambient noise interferometry can be used as an input to inversion algorithms to estimate v_s profiles of the near-surface layers. Two

different inversion procedures are carried out to obtain the velocity profiles: (1) a linearized inversion (Caiti et al., 1994) and (2) a non-linear inversion, the Adaptive Simplex Simulated Annealing (ASSA) inversion (Dosso et al., 2001). These procedures were chosen as they are well-established methods already used in various cases (see, e.g., Dong et al. (2006); Wu et al. (2020)). Additionally, we use two different inversion methods to compare their performance and estimated shear-wave velocity profiles.

Linearized Least-Squares Inversion

The linearized inversion uses the data's dispersion characteristics to determine the near-surface shear-wave model that best predicts the same observed dispersion curve. The parameters that affect the propagation of elastic waves in the near-surface layers are the compression wave velocity (v_p), the shear-wave velocity (v_s), the compression and shear Q-factor, and the density (ρ). Three assumptions are used in the inversion to simplify the inversion and forward model. The non-linear inversion minimization problem is solved using a deterministic optimization algorithm. It is initiated by a starting model, and an update is sought in the neighborhood of this model. Adding the update to the initial model, the model for the next iteration is found. This is repeated until pre-defined conditions are met. Furthermore, the linear system is solved in a least-squares sense using singular value decomposition (SVD). However, a part of the SVD is ill-conditioned, and regularization needs to be introduced. Repeating this with a reasonable starting model, the algorithm converges to the shear-wave velocity profile of the media. More information on the various aspects of the inversion can be found in Caiti et al. (1994).

In order to initiate the linearized inversion, fixed values and constraints to the P-wave velocity, the density, number of layers, and layer thickness (h) are needed, as well as an initial model of the

shear-wave velocities. In this work, six homogeneous layers plus an infinite half-space are used. The values chosen are listed in Table 3A, based on a geotechnical report by the Norwegian Geotechnical Institute (NGI; L'Heureux et al. (2015)), work by L'Heureux and Long (2017), and common P-wave velocities for clay (Sauvin et al., 2014; Salas-Romero et al., 2016). However, it is worth noting that the P-wave velocity varies depending on the clay content, porosity, water content, and overburden properties. Hence, the chosen P-wave model might vary depending on local conditions.

Adaptive Simplex Simulated Annealing (ASSA)

The non-linear inversion is a hybrid algorithm that combines local downhill simplex and simulated annealing adaptively to find the shear-wave velocities in a stratified media (Dosso et al., 2001). The ASSA algorithm uses a simplex of a pre-defined number of models and randomly perturbs the parameters after a downhill simplex step. For this, the random perturbations of the unknown parameters are used, and the trial models are either accepted or rejected according to a Metropolis criterion. After a prescribed number of perturbations, the control parameter is reduced. The process is repeated until the difference between the highest and lowest mismatch models relative to their average is less than a specified convergence factor (Li et al., 2012; Wu et al., 2020). More information on the various aspects of the inversion can be found in Dosso et al. (2001).

In the non-linear inversion, the layer thickness and shear-wave velocity in each layer are estimated parameters. In contrast, the P-wave velocity and the density of each layer are considered constant since the dispersion curves are not sensitive to these parameters. The lower and upper bounds of the estimated parameters and the fixed values of P-wave velocity and density for all the layers are listed in Table 3B. The chosen bounds are based on the NGI report (L'Heureux et al., 2015) and are chosen wide enough to capture the velocities and layer thicknesses of the subsurface.

A model with three horizontally homogeneous layers overlying an infinite half-space is chosen as the subsurface thickness model (note that the number of layers and the constraints of the layer thickness varied for some of the inversions due to the dispersion data's resolvability). The choice of the subsurface thickness model is based on the resistivity report given by Solberg et al. (2012) and tests using different models. In these tests, the inversion consistently resolves three layers which are hence used.

RESULTS AND DISCUSSION

In the following, the results from the active data using the first two modes will be presented and discussed (a discussion on the results using the other number of modes can be found in Appendix B). Subsequently, the results using the quiet periods will be presented (results from the construction noise are given in supplemental material). Then, the two will be compared, along with a time-lapse comparison between the results from the different acquisitions.

Active Data

Figure 5 shows the average dispersion images (from all images obtained in one P-wave shot series) for all acquisition days overlaid with the mean and standard deviation of the extracted dispersion curves. The curves are found by computing the dispersion image and picking the dispersion curves for each shot in a P-wave shot series. After which, the mean and standard deviation of the picked modes are calculated with an interval of 0.5 Hz. Similar to shots acquired in July, the estimated curves from all days show the same trend with four modes within a comparable frequency range ($\simeq$5-35 Hz). Furthermore, additional shots were executed outside the quick clay area on the northern segment of the array for comparison (see Figure 1C). The resulting dispersion image shows more

modes than obtained in the quick clay area, with higher frequencies and an overall higher velocity (see supplemental material for more details).

The picked dispersion curves in Figure 5 are the input data for the linearized and non-linear inversion. The inversion results using the first two modes for all acquisitions are depicted in Figure 6 (see Appendix B for inversion results using one, three, and four modes). The shear-wave velocity depth profiles are obtained by applying the constraints, fixed values, and initial models to the inversion algorithms. Figure 6A-F shows the two observed modes from every acquisition, overlaid with the predicted modes from the inversions. The fit between observed and modeled modes agrees, with some outliers at various frequencies. Figure 6G-L displays the resulting shear-wave velocity profiles, where a similar trend is seen for all days. The final v_s profiles overlay a subset of the velocity profiles used during the ASSA inversion to find the best-fitting velocity models to illustrate the uncertainty in the estimates. It is worth noting the resolution rule of thumb stating that the fundamental mode is not sensitive to variation in material properties at depths greater than $1/3$ to $1/2$ of the maximum resolved wavelength, λ_{max} (Olafsdottir et al., 2018). In the active shot data, the average maximum wavelength for the fundamental mode is 39.2 m yielding a depth resolution between 13.1 and 19.6 m. This is the trend observed in the inversion results using the fundamental mode only (Figure B-1), where the velocities below $\simeq$15 m are more spread than that for shallow depths. Similarly, the best-resolved thickness of the top layer is constrained relative to $1/3$ and $1/2$ of the shortest wavelength, λ_{min} (Olafsdottir et al., 2018). The λ_{min} range for the measured fundamental mode is 3.6 to 6.3 m, providing a possible resolution between $\simeq$1.2 to 3.2 m. For the non-linear inversion, the thickness of the first layer varies from 3 to 6 m. Moreover, higher order modes are known to resolve more of the near-surface shear-wave speed structures, penetrating deeper and providing smaller uncertainties of the estimates (Xia et al., 2003; Li et al., 2012). This effect is also observed in this work, especially prominent using two modes (see Figure 7 and Fig-

ure B-4). Note that a fixed thickness of 4 m is chosen for all layers for the linearized inversion. By investigating the obtained velocities in the different layers, there are little variations between some of the layers. Therefore, the number of layers could have been reduced, and similar results could have been obtained.

The non-linear inversion analysis provides sensitivity to each parameter. Thus, a multidimensional sensitivity (MDS) analysis can be executed using the four modes present in the data. Only the MDS using two and four modes are presented here (for the MDS of one and three modes, see Appendix B). Figure 7 illustrates that using two modes as input in ASSA produces better-resolved parameters than using four modes as two modes show more direct and narrow paths to the lowest mismatch values (except for h_3). Therefore, two modes are used hereafter. Similarly, the MDS analysis for the first two modes shows a more direct and narrow path to the lowest mismatch value for the shear-wave velocity than the thickness, suggesting better resolved v_s values. Note that the v_s profiles shown in Figure 6 (and later examples) correspond to the models with the lowest misfit in the narrow distribution of the MDS plots.

Passive Data

The inversion results for the passive data from various quiet periods are shown in Figure 8, where the observed and predicted modes are displayed in the first row, and the resulting v_s profiles, overlaid with a subset of trial v_s profiles from ASSA, in the second. The predicted dispersion curves match the observed ones (Figure 8A-C), and reliable velocity profiles are obtained. The largest wavelength for the observed dispersion varies depending on the obtained VSG. The values range from 28 to 50 m, providing an in-depth variation resolution of 9 to 25 m. The shortest wavelength ranges from 5.2 to 8 m, yielding a top-layer resolution of 1.7 to 4 m.

The associated MDS analysis is shown in Figure 9. Using the available fundamental mode for the weekend ambient noise data (2021.08.14), the velocities for all three layers are well determined. Similarly, the thickness mismatch response of layers one and two are well constrained and reliable. In contrast, the third layer thickness (h_3) has a flat response, indicating that the data cannot resolve the layer thickness.

Data Comparison and Discussion

Figure 10 summarizes the results from both the active and ambient noise data and shows that the inversion results are consistent within the measurement period. The inversion procedures produce the same pattern, where the top $\simeq$15 m are well resolved, and the layers underneath have a larger uncertainty. Figure 10A contains all four modes to compare the available information, whereas the inversion profiles in Figure 10B, C are obtained using the first two modes as these produce the best-resolved inversion parameters. Furthermore, there are minor differences between the dispersion curves extracted from the different days of active data. This can be observed in Figure 10A, where all modes are mostly within one standard deviation of each other. The fundamental modes from all quiet periods investigated are similar and give comparable velocities (Figure 10D). This suggests that the construction work, and extra load added to the quick clay, do not alter the shear-wave properties of the quick clay, and remain stable.

The shear-wave velocity profile obtained from the rock physics modeling shown in Figure 10 is consistent with the estimated velocity profiles, providing additional insight into possible rock physics parameters in the quick clay column. The change in velocity due to the additional weight introduced by the construction is estimated by a strip-load model to be 0.4 m/s at 19 m depth (see Appendix C for more details). These changes in velocity are within one standard deviation of the

dispersion curves and cannot be resolved with this method. However, this model is a conservative estimate of the potential velocity change as it assumes the minimum width and thickness of the extra road foundation and considers only the resulting stress and pressure changes. The construction work, especially the excavation activity, might add additional unwanted effects to the quick clay that needs monitoring (Bjerrum et al., 1971): (1) it might change the drainage network in the sub-surface; (2) it will break up the soil cover, which might change the erosion of the underlying material; (3) it will increase the vibrations in the ground, disturbing the bounds between the clay.

The time-lapse variation, through the distribution of the shear-wave velocities and layer interface depths presented in Figure 10, for the selected dates within the measurement period (Table 3) is summarised in Figure 11. Table 4 shows the quantified values from the active and passive data using the two inversion algorithms. Note that the estimates in the half-space are below the resolution limit and, therefore, not included in Figure 10, Figure 11 and Table 4. Furthermore, the layer interface depths found using the ASSA inversion are consistent with the input three-layered model, finding similar depth values. Based on these values and the profiles given in Figure 11C, the first layer interface may be considered to be at $\simeq$4 m, the second at $\simeq$12 m and the third at $\simeq$21 m, with the uncertainty increasing as a function of depth as highlighted by the increasing standard deviation in Table 4, also indicated by the gray shaded area in Figure 11C. Based on these results and results from previous resistivity measurements of the area (Solberg et al., 2012), the content of the different layers underneath the studied segment can be interpreted to be: (1) sedimentary crust containing agricultural soil, sand, and/or gravel, (2) marine clay, (3) quick clay. The material below 21 m is interpreted as bedrock. Note that the resistivity profiles given by Solberg et al. (2012) show a significant lateral variation in the depth and thickness of the quick clay layer; hence the layer interpretation will vary along the cable profile (for an example, see supplemental Material). For this particular segment, the maximum depth range for shear-wave velocity is $\simeq$15 m, and Solberg et al.

(2012) have shown the quick clay layer under the studied profile to be at a depth of roughly 10 m to 20 m. For situations like this, the procedure needs further development to obtain more reliable shear-wave velocity values for depths below 15 m. One possibility is using an alternative seismic source generating lower frequencies that penetrate deeper. The surface waves will then be able to capture changes occurring in the deeper portions of the quick clay layers. However, the resolution obtained in this study is sufficient for observing changes within the top 15 m.

The distribution of the velocities from the two inversion methods are given in Figure 11B, D, color-coded based on the layer in which the velocities are estimated. The velocity profiles from the various acquisition dates are similar, with a velocity distribution in agreement with a three-layer model and an expected increase in uncertainty with depth. Note that the choice of the bedrock interface has considerable uncertainty. This is visible in the shaded gray area of Figure 11A, C and affirmed by the rule of thumb for depth resolution (Olafsdottir et al., 2018). Ultimately, this interface location is chosen based on the results of this study and constrained by the resistivity survey by Solberg et al. (2012).

All modes are within one standard deviation of each other, yet minor time-lapse effects are present in the data. The dispersion curves from 2021.09.15 show some deviation from the other curves for mode two in the frequency range 20-25 Hz. The soil is reported as wet during this acquisition, and the shots are obtained during noisy construction activity. The wet soil is unlikely to increase the phase velocities as there are other acquisition dates with a higher humidity level that did not show the same trend (see supplemental Figure S4). In addition, changes between dry, wet, and cold periods could not be resolved in the data. The reason is believed to be due to a very thin weather zone of maybe $\simeq$0.5-1 m. The non-linear inversion, and the shortest wavelength in the dispersion curves, resolve a minimum thickness of $\simeq$3 m for the first layer. The estimated velocity in the layer will be an average of the material velocities within, which attenuates the weather-induced

changes. Hence, the surface waves cannot resolve the weather changes due to the frequency bandwidth. Other explanations for the observed time-lapse change are variations in the sledgehammer shots and/or influence from the background noise level. Effects from these are evident through the variation in dispersion curves from 2021.09.15, as indicated by the wider error bars in Figure 5C. For most acquisition days, the shots produce no or minimal variation in the dispersion curves. The biggest differences are found in the extreme frequency values for each mode (see Figure 5). Therefore, it is concluded that most of the time-lapse variations in the dispersive data are caused by non-repeatability effects. Nevertheless, the shear-wave velocity profile obtained provides reference trends for the quick clay at undisturbed conditions. This agrees with *in situ* observations from the study area throughout the fieldwork, where no changes to the quick clay area are observed. Moreover, changes during failure of quick clay are dramatic where its shear strength, and the shear-wave velocity, will decrease towards zero. It is anticipated that changes leading to such conditions will be observable through the proposed methods. However, two problems are not possible to address in this work. (1) The time scale at which failure might occur. For the Gjerdrum quick clay avalanche in 2020 (Ryan and Riekeles, 2021) it was possible to compute the minimum time duration of the avalanche based on witness observations and the exact time when the fiber- and power-cable broke along with when the avalanche stopped. The minimum duration was found to be eleven minutes. However, the changes to the subsurface before the avalanche broke the cables could not be estimated for the event. (2) Deduction of the shear-wave velocity bounds for when the quick clay becomes unstable. Developing an automated shot system will make it possible to find the shear-velocity profiles in near-real-time and make it possible to estimate the shear-wave velocity profile within eleven minutes (assuming a similar time duration as in Gjerdrum). This is not the case for the passive data where at least 22 hrs of recordings are needed to find stable VSGs, maybe less for periods with extreme weather conditions. Another possibility is to take advantage of the surface wave generated

by the road construction directly as described by Yuan et al. (2020) and use it as a mobile active source.

Both inversion algorithms produce comparable shear-wave velocity depth profiles and can be used in the proposed monitoring system either together or individually. There are clear advantages and disadvantages to linearized and non-linear inversions. Normally, linearized inversion is less computationally demanding than non-linear inversion. However, the initial values in the linearized inversion are crucial for finding the global minimum, which is circumvented in the non-linear inversion by employing a hybrid method with some pre-defined constraints. In addition, the non-linear inversion carries out a sensitivity analysis for the estimated shear-wave velocities and layer thicknesses, providing additional information on how well the different values are estimated. In this study, *a prior* information from the NGI report (L'Heureux et al., 2015) is available, providing information for the initial parameterization. When such information is available, the linearized model converges to a stable solution and is therefore preferred due to the low computational cost. However, when the quick clay properties change during an event, the initial model will no longer be accurate, and there is a risk of incorrect and/or unstable inversion results. In such cases, the non-linear method is preferred. Therefore, it is recommended to use a combination of the two. Initially, the linearized method would suffice when there is only natural variation of the subsurface properties, as observed in this study. Subsequently, when the subsurface characteristics vary, the non-linear method (independent of an initial model) should be utilized. This allows for an accurate shear-wave velocity model or an updated initial model to be used in the linearized approach.

CONCLUSION

This work demonstrates the possibilities of establishing an early-warning system based on time-lapse analysis of shear wave velocities using fiber-optic cables trenched into the shallow soil layer of a known quick clay area in Norway. Exploiting data recorded by DAS, elastic monitoring with high spatial coverage and resolution has been shown to be feasible. By acquiring both active and passive data before, during, and after a road construction period, it is possible to extract clear Rayleigh wave dispersion using both data-sets. These dispersion curves are then used as input to two different inversion algorithms, a linearized least-squares inversion, and the adaptive simplex simulated annealing inversion algorithm, to compare their performance and the estimated shear-wave velocity profiles. Both inversion algorithms find reliable velocity profiles down to a depth of $\simeq$15 m. Moreover, the inversion methods produce similar results using both active and passive data and could be combined in the early-warning system as they complement each other's limitations. The dispersion curves of the surface waves and the obtained shear-wave velocity profiles for both the active and passive data did not change significantly during the acquisition period, suggesting that the quick clay properties remained stable as the road construction proceeded. Nevertheless, the obtained results provide reference shear-wave velocity trends for the study area in undisturbed conditions. This provides valuable information for future comparison to potential failure scenarios. Moreover, the passive data displayed a larger deviation in the picked phase velocities and fewer dispersive modes than the active data. The increased spread in the dispersion curves for the passive data is most likely due to additional noise sources generating energy broadside to the array, producing Love waves in addition to Rayleigh waves.

The results in this work illustrate the feasibility of using both active and passive data, both together and separately, recorded on fiber-optic cables in an early-warning system for quick clay

avalanches. However, the main limitation is the depth resolution. Recording data on fiber-optic cables is a cost-efficient and easy way of setting up the system for long-term monitoring, as the cable might already be in the quick clay, and all that is needed is to connect an interrogator unit.

ACKNOWLEDGMENTS

We thank the Norwegian Research Council and the industry partners of the GAMES consortium at NTNU for the financial support (grant no. 294404) and the Centre for Geophysical Forecasting at NTNU (grant no. 309960). Furthermore, we want to thank Jonas Dybdahl for permission to use his barn for the instrumentation and Hans Henrik Horneman for permission to trench fiber cables on his land. Norconsult assisted in the drilling of two observation wells, and Bjørnar Buhaug (mayor, Indre Fosen), Tore Solli (Indre Fosen), Olaf Rovik (Trøndelag Fylkeskommune), Emil Cederstrøm (Norconsult) and Kristian Aune (Norconsult) are all acknowledged for help and assistance in the planning of these experiments. Finally, we thank the reviewers for the many excellent and helpful comments that significantly improved the work and the paper.

APPENDIX A

THE EFFECT OF DIFFERENT GAUGE LENGTHS

To better understand the effect the Gauge Length (GL) has on the resolution of the surface wave analysis, a follow up survey was carried out on 2022.03.22, acquiring sledgehammer shots using different GL. During the survey, four different lengths were investigated; 2 m, 4 m, 6 m, and 8 m. These do not include the 3 m GL presented throughout the paper. Figure A-1 shows two clear effects (see Figure 5 for similar plots using 3 m GL): (1) shorter GL captures shorter wavelength. Using a 2 m gauge length, more frequencies can be observed for each dominant velocity. In the 8 m GL case, the short wavelengths are not observed. This wavelength high-pass filtering is especially clear for the fundamental mode. For a 2 m GL, the minimum wavelength observed is 2.94 m, compared to 5.56 m for 4 m GL, 7.14 m for 6 m GL, and 10 m for 8 m GL. Previously it has been shown that when the wavelength recorded approaches the GL, the signal significantly distorts (Hartog, 2017). This is also observed in Figure A-1 (where the black line denotes this limit, $f = v_{phase}/GL$), where the majority of the modes can not be observed close to this line. (2) Longer GL contains stronger arrivals for higher velocities.

APPENDIX B

THE EFFECTS OF USING DIFFERENT NUMBER OF MODES

The effects of using a different number of modes are presented and discussed. In addition to using two modes in the inversion (see Figures 6), one (Figures B-1), three (Figure B-2) and four (Figure B-3) modes have also been investigated. The inversion results show similar shear-wave velocity profiles, with some variations. These differences are also evident in the multidimensional sensitivity

(MDS) analysis presented in Figure B-4 and Figure 7 through the differences in the shape of the individual scatter plots. There are various factors producing these variations. The first is related to the different input data to the inversions when increasing the number of modes. This should, in general, improve the resolution of the near-surface shear-wave speed structures, penetrating deeper and providing smaller uncertainties of the estimates (Xia et al., 2003; Li et al., 2012). While this is the case when two modes are used, applying three and four modes produces worse sensitivity for most inverted parameters. Previous work by Li et al. (2012) shows an example where Love and Rayleigh wave modes in close proximity give inaccurate dispersion curves that are inappropriate for inversion and lead to biased velocity profiles. In this study, modeled Love and Rayleigh wave modes (using the v_s profile estimated using two modes from 2021.08.12) are close to each other (Figure A-3). The excited Love wave may have contaminated the extracted Rayleigh wave dispersion curves, which might bias the inversion results.

APPENDIX C

ROCK PHYSICS MODELING

For comparing the estimated shear-wave velocity profiles through the time-laps surface wave inversion at the Rissa site, an S-wave velocity depth profile is calculated using the empirical equation of Hardin and Blandford (1989) where the elastic shear modulus for the vertical direction (c_{44}) is given as:

$$c_{44} = \frac{OCR^k}{(0.3 + 0.7e^2)} \frac{S_{44}}{(2 + 2\nu)} p_{ref}^{(1-n)} (\sigma'_v \sigma'_h)^{n/2} \tag{C-1}$$

The model parameters assumed for simulating the shear modulus depth profile are given in Table 5. The predicted elastic shear modulus is in the plane containing the principal stresses in vertical and horizontal directions. Figure C-1A shows the assumed principal differential stress profiles in ver-

tical (σ'_v) and horizontal (σ'_h) directions when considering hydrostatic pore pressure. Moreover, Figure C-1B displays the simulated void ratio reduction expected across the quick clay column overlaid with values from lab analysis of quick clay samples from Flotten, Norway. The coefficient of earth pressure at rest ($K_0 = \sigma'_h/\sigma'_v$) is kept constant ($\simeq$0.66) when assuming a friction angle, based on comparable clay material from Gella (2017). The clay is modeled as normally consolidated with an over-consolidation ratio (OCR) equal to one. That is, the *in situ* vertical differential stress is about equal to the past maximum vertical differential stress. A more detailed explanation of the model and its parameters and assumptions can be found in Hardin and Blandford (1989). Furthermore, the shear wave velocity (v_{sv}) is computed as

$$v_{sv} = \sqrt{\frac{c_{44}}{\rho_b}} \tag{C-2}$$

when assuming 100% water saturation. The shear wave is assumed to propagate in the vertical direction along the z-axis, with the particle motion horizontally along the x-axis. The bulk density (ρ_b) is calculated as a volume-weighted average between the mineral and pore fluid densities (see Table 5). The resulting predicted shear modulus is depicted in Figure C-1C and the corresponding shear-wave velocity depth profile, given the specific *in situ* conditions for a 25 m thick quick clay column, in Figure C-1D.

In addition to modeling the shear-wave velocity profile, the effect of the applied surface load caused by the new road foundation is investigated using the analytical expression of Boussinesq (1885). Under the assumption of uniform strip load, the vertical total and effective stress changes are estimated as a function of the depth of the 19 m deep well-bore located 30 m from the edge of the new road foundation. The foundation has a minimum width of 30 m and a minimum thickness of about 2.4 m with an assumed bulk density of 1660 kg/m^3. This results in an estimated vertical stress increase of 39 kPa underneath the road stip. The vertical stress change ($\Delta\sigma_z$) can then be

computed:

$$\Delta\sigma_z = \frac{q}{\pi}(\alpha + \sin(\alpha)\cos(\alpha + 2\beta)) \tag{C-3}$$

where q is the load per unit area introduced by the road, α the angle between the far end of the foundation and a position along the well-bore make, whereas β is the angle between the closest point of the foundation and the position along the well-bore. The vertical stress change at 19 m depth in the well location is estimated to be about 1.2 kPa (see Figure C-1E), which corresponds to a shear-wave velocity increase of about 0.4 m/s or no change in the shear velocity. In addition to comparing the shear-wave velocities to rock physics, the profiles are compared to an ultrasound test of a $30\times50\times20$ cm^3 sample extracted from the survey area (from a depth of $\simeq$40 cm). Laboratory investigation showed a velocity of 160 m/s using a 100 kHz input signal and a high attenuation level, where the output center frequency decreased to $\simeq$15 kHz.

REFERENCES

Bensen, G., M. Ritzwoller, M. Barmin, A. L. Levshin, F. Lin, M. Moschetti, N. Shapiro, and Y. Yang, 2007, Processing seismic ambient noise data to obtain reliable broad-band surface wave dispersion measurements: Geophysical Journal International, **169**, 1239–1260.

Bjerrum, L., T. Løken, S. Heiberg, and R. Foster, 1971, A field study of factors responsible for quick clay slides: , 17–26.

Bouffaut, L., K. Taweesintananon, H. J. Kriesell, R. A. Rørstadbotnen, J. R. Potter, M. Landrø, S. E. Johansen, J. K. Brenne, A. Haukanes, O. Schjelderup, et al., 2022, Eavesdropping at the speed of light: distributed acoustic sensing of baleen whales in the arctic: Frontiers in Marine Science, 994.

Boussinesq, J., 1885, Application des potentiels à l'étude de l'équilibre et du mouvement des solides élastiques: principalement au calcul des déformations et des pressions que produisent, dans ces solides, des efforts quelconques exercés sur une petite partie de leur surface ou de leur intérieur: mémoire suivi de notes étendues sur divers points de physique, mathematique et d'analyse: Gauthier-Villars, **4**.

Caiti, A., T. Akal, and R. D. Stoll, 1994, Estimation of shear wave velocity in shallow marine sediments: IEEE Journal of Oceanic Engineering, **19**, 58–72.

Cheng, F., B. Chi, N. J. Lindsey, T. C. Dawe, and J. B. Ajo-Franklin, 2021, Utilizing distributed acoustic sensing and ocean bottom fiber optic cables for submarine structural characterization: Scientific reports, **11**, 1–14.

Dong, H., J. M. Hovem, and Å. Kristensen, 2006, Estimation of shear wave velocity in shallow marine sediment by multi-component seismic data: a case study: Procs. of the 8th European Conference on Underwater Acoustics, 497–502.

Dosso, S. E., M. J. Wilmut, and A.-L. Lapinski, 2001, An adaptive-hybrid algorithm for geoacoustic

inversion: IEEE Journal of Oceanic Engineering, **26**, 324–336.

Dou, S., N. Lindsey, A. M. Wagner, T. M. Daley, B. Freifeld, M. Robertson, J. Peterson, C. Ulrich, E. R. Martin, and J. B. Ajo-Franklin, 2017, Distributed acoustic sensing for seismic monitoring of the near surface: A traffic-noise interferometry case study: Scientific reports, **7**, 1–12.

GEBCO, C. G., 2021, Gebco 2021 grid.

Gella, K., 2017, Geotechnical and geological charaterisation of a quick clay site at flotten.

Google, M., 2022, Overview map Rissa, Norway. (Accessed: 2022-02-04).

Gregersen, O., et al., 1981, The quick clay landslide in rissa, norway: Norwegian Geotechnical Institute Publication, **135**, 1–6.

Hardin, B. O., and G. E. Blandford, 1989, Elasticity of particulate materials: Journal of Geotechnical Engineering, **115**, 788–805.

Hartog, A. H., 2017, An Introduction to Distributed Optical Fibre Sensors, 1 ed.: CRC Press.

Kähler, S., and R. Meissner, 1983, Radiation and receiver pattern of shear and compressional waves as a function of poisson's ratio: Geophysical Prospecting, **31**, 421–435.

Landrø, M., L. Bouffaut, H. J. Kriesell, J. R. Potter, R. A. Rørstadbotnen, K. Taweesintananon, S. E. Johansen, J. K. Brenne, A. Haukanes, O. Schjelderup, et al., 2022, Sensing whales, storms, ships and earthquakes using an Arctic fibre optic cable: Scientific Reports, **12**, 1–10.

L'Heureux, J.-S., M. Long, and T. Lunne, 2015, Korrelasjoner mellom skjærbølgehastighet og geotekniske parametere i Norsk leirer, SP8-GEODIP.

Li, C., S. E. Dosso, H. Dong, D. Yu, and L. Liu, 2012, Bayesian inversion of multimode interface-wave dispersion from ambient noise: IEEE Journal of Oceanic Engineering, **37**, 407–416.

Lindsey, N. J., E. R. Martin, D. S. Dreger, B. Freifeld, S. Cole, S. R. James, B. L. Biondi, and J. B. Ajo-Franklin, 2017, Fiber-optic network observations of earthquake wavefields: Geophysical Research Letters, **44**, 11–792.

Long, M., A. Trafford, T. McGrath, and P. O'Connor, 2020, Multichannel analysis of surface waves (masw) for offshore geotechnical investigations: Engineering Geology, **272**, 105649.

Lundström, K., R. Larsson, and T. Dahlin, 2009, Mapping of quick clay formations using geotechnical and geophysical methods: Landslides, **6**, 1–15.

L'Heureux, J.-S., and M. Long, 2017, Relationship between shear-wave velocity and geotechnical parameters for norwegian clays: Journal of geotechnical and Geoenvironmental engineering, **143**, 04017013.

Matsumoto, H., E. Araki, T. Kimura, G. Fujie, K. Shiraishi, T. Tonegawa, K. Obana, R. Arai, Y. Kaiho, Y. Nakamura, et al., 2021, Detection of hydroacoustic signals on a fiber-optic submarine cable: Scientific reports, **11**, 1–12.

Mestayer, J., B. Cox, P. Wills, D. Kiyashchenko, J. Lopez, M. Costello, S. Bourne, G. Ugueto, R. Lupton, G. Solano, et al., 2011, Field trials of distributed acoustic sensing for geophysical monitoring, *in* Seg technical program expanded abstracts 2011: Society of Exploration Geophysicists, 4253–4257.

NGI, 2011, The Quick Clay Landslide at Rissa - 1978 (english commentary). (Accessed: 2022-01-24).

Olafsdottir, E. A., B. Bessason, and S. Erlingsson, 2018, Combination of dispersion curves from masw measurements: Soil Dynamics and Earthquake Engineering, **113**, 473–487.

Rivet, D., B. de Cacqueray, A. Sladen, A. Roques, and G. Calbris, 2021, Preliminary assessment of ship detection and trajectory evaluation using distributed acoustic sensing on an optical fiber telecom cable: The Journal of the Acoustical Society of America, **149**, 2615–2627.

Rodríguez Tribaldos, V., and J. B. Ajo-Franklin, 2021, Aquifer monitoring using ambient seismic noise recorded with distributed acoustic sensing (das) deployed on dark fiber: Journal of Geophysical Research: Solid Earth, **126**, e2020JB021004.

Ryan, I., and H. Riekeles, 2021, Årsaken til kvikkleireskredet i gjerdrum 2020.

Salas-Romero, S., A. Malehmir, I. Snowball, B. C. Lougheed, and M. Hellqvist, 2016, Identifying landslide preconditions in swedish quick clays—insights from integration of surface geophysical, core sample-and downhole property measurements: Landslides, **13**, 905–923.

Sauvin, G., I. Lecomte, S. Bazin, L. Hansen, M. Vanneste, and J.-S. L'Heureux, 2014, On the integrated use of geophysics for quick-clay mapping: The hvittingfoss case study, norway: Journal of Applied Geophysics, **106**, 1–13.

Schimmel, M., and H. Paulssen, 1997, Noise reduction and detection of weak, coherent signals through phase-weighted stacks: Geophysical Journal International, **130**, 497–505.

Shragge, J., J. Yang, N. Issa, M. Roelens, M. Dentith, and S. Schediwy, 2021, Low-frequency ambient distributed acoustic sensing (das): case study from perth, australia: Geophysical Journal International, **226**, 564–581.

Solberg, I.-L., E. Dalsegg, and J.-S. L'Heureux, 2012, Resistivitetsmålinger for løsmassekartlegging ved rein kirke i rissa, sør-trøndelag. data og tolkninger.

Taweesintananon, K., M. Landrø, J. K. Brenne, and A. Haukanes, 2021, Distributed acoustic sensing for near-surface imaging using submarine telecommunication cable: A case study in the trondheimsfjord, norway: Geophysics, **86**, B303–B320.

Verschuur, D. J., 2013, Seismic multiple removal techniques: past, present and future: EAGE publications Houten, The Netherlands.

Waagaard, O. H., E. Rønnekleiv, A. Haukanes, F. Stabo-Eeg, D. Thingbø, S. Forbord, S. E. Aasen, and J. K. Brenne, 2021, Real-time low noise distributed acoustic sensing in 171 km low loss fiber: OSA Continuum, **4**, 688–701.

Wu, G., H. Dong, G. Ke, and J. Song, 2020, Shear-wave tomography using ocean ambient noise with interference: Remote Sensing, **12**, 2969.

Xia, J., R. D. Miller, C. B. Park, and G. Tian, 2003, Inversion of high frequency surface waves with fundamental and higher modes: Journal of Applied Geophysics, **52**, 45–57.

Yuan, S., A. Lellouch, R. G. Clapp, and B. Biondi, 2020, Near-surface characterization using a roadside distributed acoustic sensing array: The Leading Edge, **39**, 646–653.

LIST OF TABLES

LIST OF FIGURES

5 Average phase velocity spectrum from one active shot series from different days overlaid with mean and one standard deviation computed using the four extracted dispersion curves.

6 Observed and predicted dispersion curves for two modes from active data and the associated inversion results. (A-F) The fit between the observed (black) and the predicted (red for linearized, blue for ASSA) dispersion curves. (G-L) The estimated shear-wave velocity profiles from the linearized (L; red) and ASSA non-linear (NL; blue) inversion overlay a subset of the velocity profiles (black) generated by the ASSA inversion. The ensemble illustrated the uncertainty of the parameter estimation.

7 Multidimensional sensitivity analysis using two and four modes for active shot data 2021.08.12. (A-C) Shear-wave velocity for layers 1-3 using two modes. (D-F) Shear-wave velocity for layers 1-3 using four modes. (G-I) Thickness for layers 1-3 using two modes. (J-L) Thickness for layers 1-3 using four modes. The mismatch gives the normalized difference between observed and predicted data given as values between 0 and 1.

8 Same as Figure 6 but for the inversion of one mode obtained from the ambient noise interferometry.

9 Multidimensional sensitivity analysis for ambient noise data on 2021.08.14. (A-C) Shear-wave velocity for layers 1-3. (D-F) Thickness for layers 1-3.

10 Dispersion curves and inversion results from active shots (A-C) and ambient noise interferometry (D-F). (A) The mean dispersion curves from the different shot days with error bars indicate one standard deviation. (B) The linearized inversion profiles using two modes. (C) The ASSA inversion profiles using two modes. (D) Dispersion curves from the interferometry. (E-F) The linearized and ASSA inversion profiles, respectively. (B, C, E, F) are all overlaid with the predicted v_s profile from the rock physics modeling (see Appendix C for more details).

11 Time-lapse analysis of the inversion profiles for the active and passive data over the seven-

month acquisition period. (A) Velocity profiles obtained from the linearized inversion for the active (red) and passive data (blue) with mean profile (black) and one standard deviation (std) over velocity profiles found using active and passive data, indicating the variation over the acquisition period (gray shaded area). Note that the time-lapse of shear-wave velocity profiles have not been separated by color (see Figure 10). (B) Associated velocity distribution with N_L velocity values from the linearized inversion, color-coded by the interpreted layers. (C) and (D) are the same as (A) and (B) but from ASSA inversion with N_{NL} velocity values. (E) Associated depth distribution with N_{NL} depth values from the non-linear inversion. The layers are interpreted from (E), indicated as solid lines for the layers within the resolution rule of thumb, and dashed when outside. For an overview of the individual estimated values from the active and passive data, see Table 4.

A-1 Comparison of dispersion images from data using different gauge lengths (GL). The black line is computed as the case when the wavelength is equal to GL, i.e., $f = v_{phase}/GL$.

B-1 Observed and predicted dispersion curves for one mode from active data and the associated inversion results. (A-F) The fit between the observed (black) and the predicted (red for linearized, blue for ASSA) dispersion curves. (G-L) The estimated shear-wave velocity profiles from the linearized (L; red) and ASSA non-linear (NL; blue) inversion overlay a subset of the velocity profiles (black) generated by the ASSA inversion. The ensemble illustrated the uncertainty of the parameter estimation.

B-2 Same as Figure 6 and Figure B-1 but for the inversion of three modes.

B-3 Same as Figure 6 and Figure B-1 but for the inversion of four modes.

B-4 MDS from 2021.08.12 for one mode (A-C and G-I) and three modes (D-F and J-L).

C-1 Stress (A) and void ratio (B) depth profiles as a function of depth are used in estimating the shear modulus depth trend at the Rissa acquisition site when assuming hydrostatic pore pressure conditions. In (B), the green dots represent the average bulk density estimated from lab analysis

of quick clay samples of the Tiller site in Trondheim, Norway. (C) The predicted shear modulus depth profile using the model of equation C-1. (D) The corresponding synthetic shear wave velocity depth profile (orange) along with NGI's fitted regression line is based on 138 clay cores (black) acquired from central- and eastern-Norway (L'Heureux et al., 2015). (E) The vertical stress change as a function of depth is estimated using the strip-load model (Boussinesq, 1885).

Citation	DAS	Active data	Passive data	Geology	Time-lapse	# modes
This paper	x	Sledgehammer	x	Quick clay	x	1-4
Dou et al. (2017)	x		x	NA	x	1-2
Shragge et al. (2021)	x		x	Sediments		1
Olafsdottir et al. (2018)		Seismic shots		Silty sand		1
Martin et al. (2016)	x		x	Permafrost	x	1
Zeng et al. (2017)	x	Frequency sweep	x			
Martin and Biondi (2017)	x		x	NA	x	NA
Ajo-Franklin et al. (2019)	x		x	Sediments	x	1-3
Spica et al. (2020)	x		x	Sediments		1-2
Renalier et al. (2010)		Sledgehammer & Explosive sources	x	Clayey deposits	x	1
Song et al. (2021)	x	Vibroseis	x	NA		1
Maraschini and Foti (2010)		Weight drop Sledgehammer		Sediments clayey sands		1-4
Arisona et al. (2017)		Seismic shots		Sediments		
Yuan et al. (2020)	x		Traffic Earthquake			2

Table 1: Content of this paper compared to other publications.

Data type	Date	Cable length (km)	Spatial Sample rate (m)	Gauge length (m)	Shots #	Periods analyzed
A	2021.07.01	8	1	4	1170	X
P	2021.07.05-07.24 2021.08.10-08.12	6	2	3	– –	– –
A	2021.08.12	6	2	3	250	X
P	2021.08.12-08.20 2021.09.08-09.15	6 8	2 2	3 3	- -	2021.08.14, 08.18 –
A	2021.09.15	8	2	3	73	X
P	2021.09.18-11.02	8	2	3	-	2021.09.18-19, 09.22 2021.10.09-10
A	2021.11.02	8	2	3	212	–
P	2021.11.02-11.30	8	2	3	–	X
A	2021.12.01	8	2	3	214	X
P	2021.12.16-12.23 2022.01.04-01.14 2022.01.17-02.02	8	2	3	– – –	– – –
A	2022.02.02	8	2	3	340	X
A	2022.03.22	8	1	2, 4, 6, 8	480	X

Table 2: Acquisition parameters and periods for the data. All data are acquired with a temporal sampling rate of 1000 Hz. Note that the acquisition on 2022.03.22 is solely to investigate the effect of changing the gauge length and is not part of the monitoring study. A = active data, P = passive data.

(A)	Linearized Inversion			
Layer	v_p (m/s)	ρ (kg/m^3)	$v_s^{(0)}$ (m/s)	Thickness, h (m)
1	600	1.825	100	4
2	770	1.85	130	4
3	930	1.875	160	4
4	1100	1.9	190	4
5	1270	1.925	220	4
6	1430	1.95	250	4
7	1600	2.0	280	4
(B)	ASSA			
Layer	v_p (m/s)	ρ (kg/m^3)	v_s (m/s)	Thickness, h (m)
1	600	1.825	0-300	0-10
2	933	1.883	0-350	0-40
3	1266	1.942	0-500	0-40
4	1600	1.9	0-650	0-50

Table 3: (A) Fixed and initial values used in the linearized inversion. (B) Fixed values and con-straints for ASSA.

Linearized Inversion		
Depth (m)	v_s (m/s)	
	A	P
4.0	105±2	105±2
8.0	156±4	160±2
12.0	167±9	173±3
16.0	199±12	201±6
20.0	233±17	224±18
24.0	263±34	239±28
28.0	285±49	248±35

ASSA			
Depth (m)		v_s (m/s)	
A	P	A	P
3.3±0.8	4.1±0.3	98±8	107±5
9.5±2.7	13.0±0.9	151±8	163±2
26.4±6.7	30.2±9.3	201±28	243±27

Table 4: Statistical overview of estimated values for the two inversion algorithms applied to the active (A) and passive (P) data. The mean and the standard deviation are computed for each layer.

Variables	Description	Values
OCR	Over-consolidation-ratio	1.00
k	Dependent on the plasticity index of the soil	0.30
e	Void ratio or pore volume	Void ratio depth profile (Figure C1B)
ν	Poisson's ratio for wet conditions	0.48
S_{44}	Dimensionless elastic stiffness coefficient	1400.00
n	Stress coefficient	0.50
p_{ref}	Atmospheric pressure	$\simeq$101.31 kPa
ρ_m	Density of mineral material	2.75 g/cm^3
ρ_p	Density of pore water	1.00 g/cm^3

Table 5: Modeling parameters used in predicting the elastic shear modulus depth profile as shown in Figure C-1.

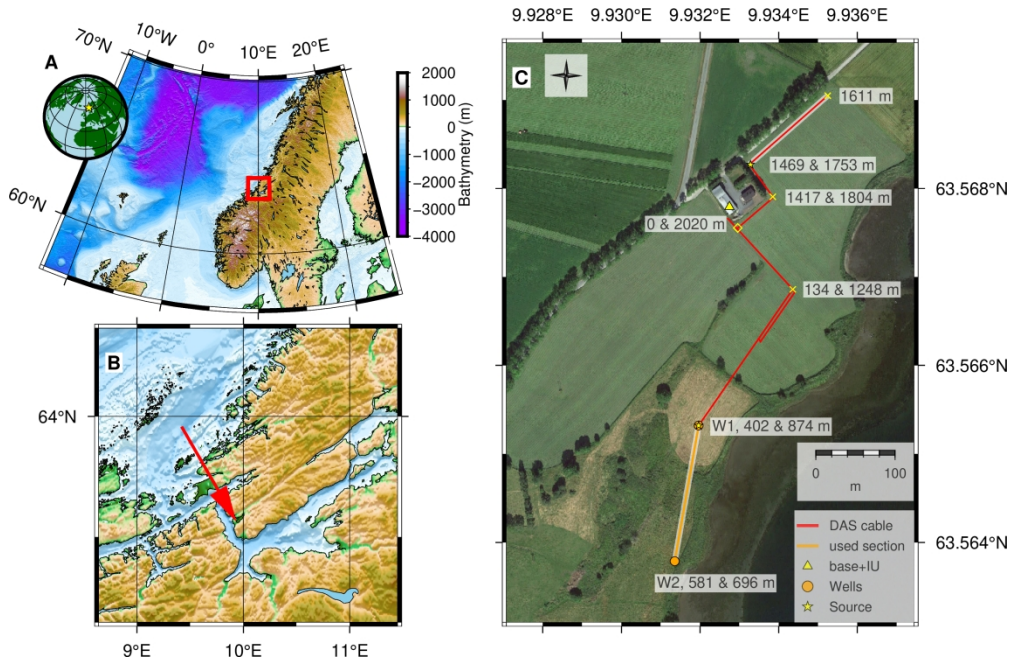

Figure 1: (A-B) Overview map indicating the study area, Rissa, in Norway (background map from GEBCO (2021)). (C) Layout and annotation of the DAS fiber-optic cable (red line). The orange highlighted section depicts the segment inside the quick clay area used in the analysis in this paper. The red highlighted (northern) section indicates the section used to analyze the area outside the quick clay area. The annotations show the distances along the cable for a selection of segments. Note that only the distances for the first route are depicted. Yellow crosses indicate the cable portion corresponding to the distance marking, and the yellow square indicates the point at which the laser enters the northern part of the cable (satellite image from Google (2022)).

466x302mm (177 x 177 DPI)

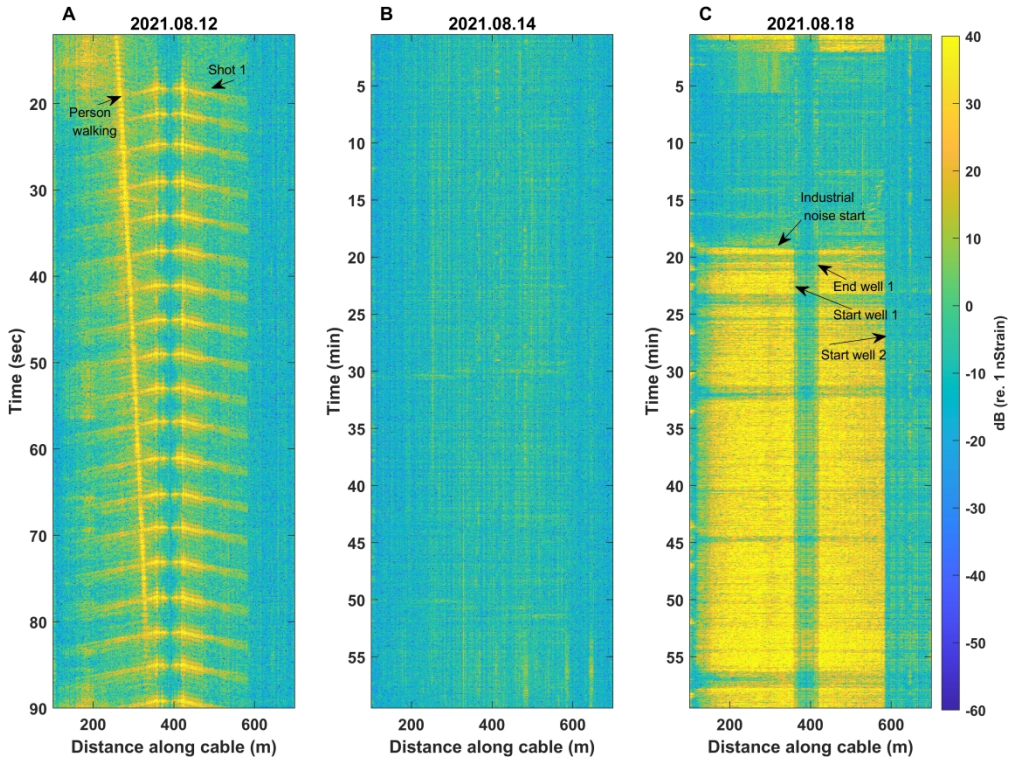

Figure 2: Observed data for three different days during the acquisition period in August 2021. (A) Shots from a shot series in 2021.08.12. Two signals are evident. The first is the repeating shots, and the second is a person walking along the cable (the linear event, the slope gives a speed of ≃4 km/h). In (B) and (C), two different days of ambient noise are depicted, without (B) and with (C) construction work. The ambient noise without construction, referred to as quiet periods, shows only isotropic noise. In the period with construction noise, it is evident when the work is ongoing (higher amplitudes) and when there are breaks (lower amplitudes, similar to amplitudes in B).

677x507mm (177 x 177 DPI)

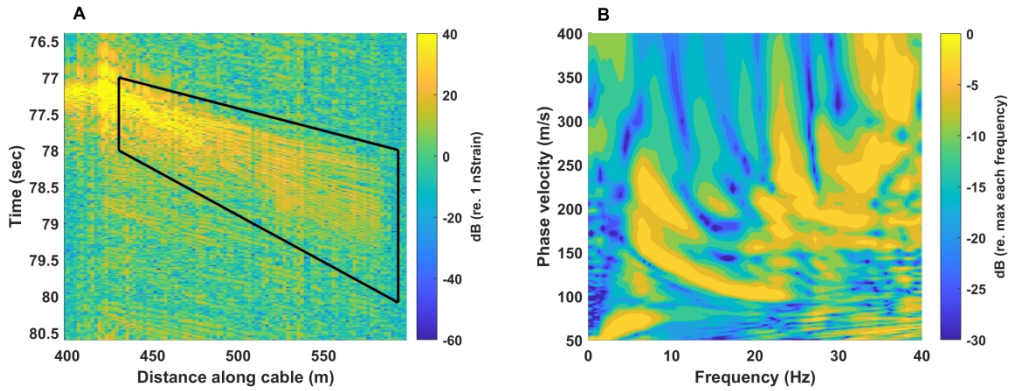

Figure 3: (A) One observed shot from 2021.08.12 with the area used to compute the dispersion image indicated (black trapezium). (B) Resulting dispersion image. Each frequency is normalized by its maximum.

705x269mm (118 x 118 DPI)

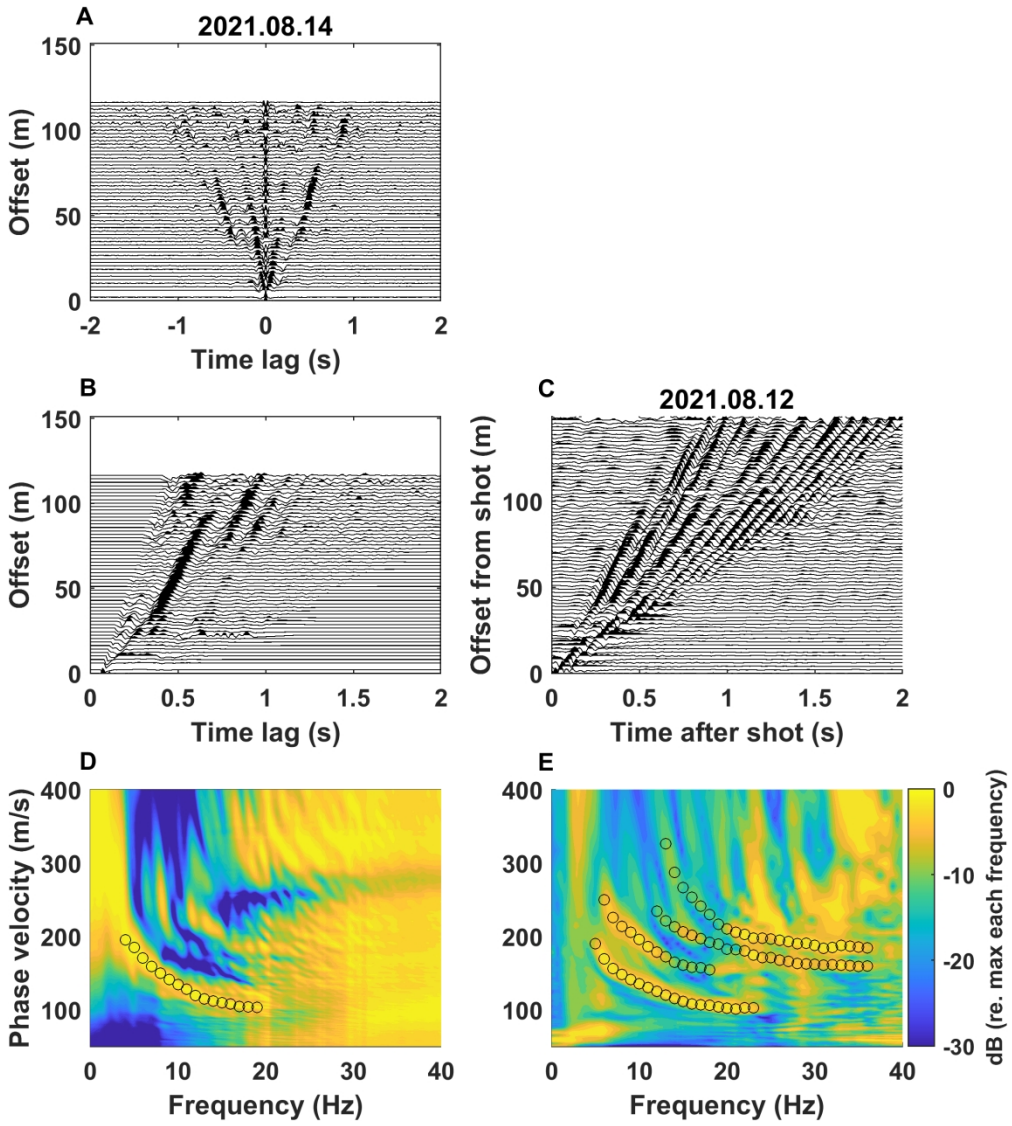

Figure 4: Virtual shot gathers and resulting dispersion images for 2021.08.14 (column one). A shot from 2021.08.12 for comparison (column two). (A) The two-sided VSG. (B) Muted one-sided VSG, i.e., the average of positive and negative time lags from the two-sided VSG. (C) Observed dispersion arrivals from one shot, 2021.08.12. (D-E) The resulting dispersion image overlaid with the extracted Rayleigh wave dispersion curves (black circles).

510x569mm (118 x 118 DPI)

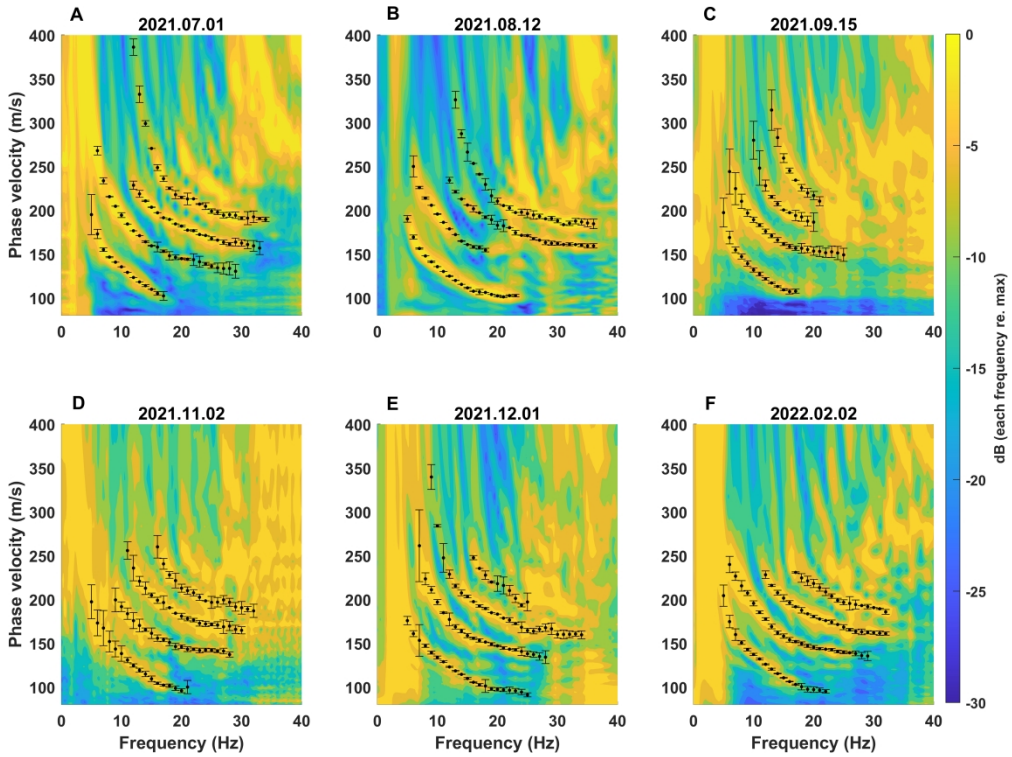

Figure 5: Average phase velocity spectrum from one active shot series from different days overlaid with mean and one standard deviation computed using the four extracted dispersion curves.

682x509mm (177 x 177 DPI)

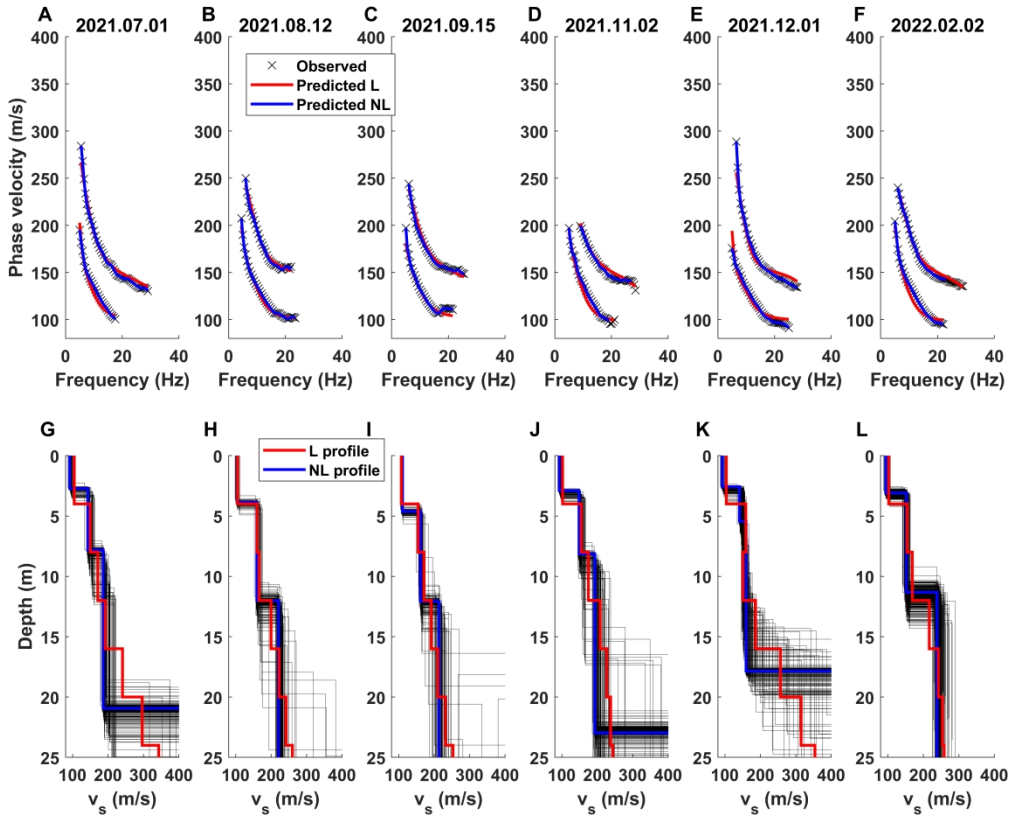

Figure 6: Observed and predicted dispersion curves for two modes from active data and the associated inversion results. (A-F) The fit between the observed (black) and the predicted (red for linearized, blue for ASSA) dispersion curves. (G-L) The estimated shear-wave velocity profiles from the linearized (L; red) and ASSA non-linear (NL; blue) inversion overlay a subset of the velocity profiles (black) generated by the ASSA inversion. The ensemble illustrated the uncertainty of the parameter estimation.

633x512mm (177 x 177 DPI)

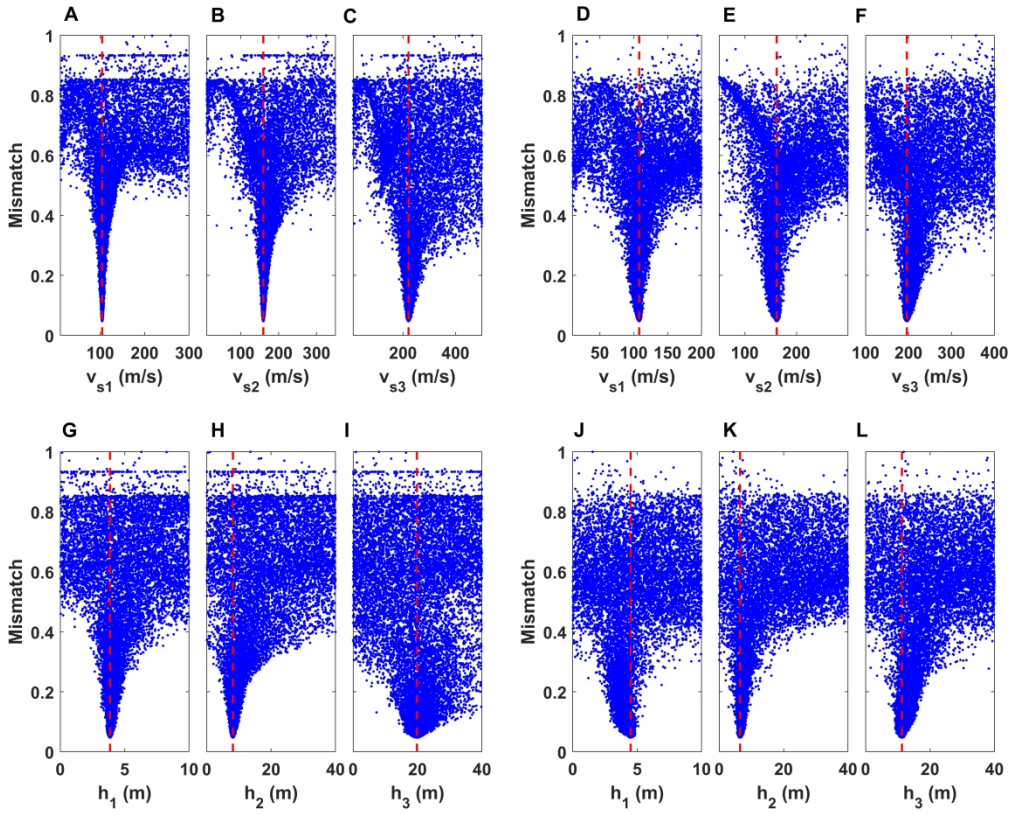

Figure 7: Multidimensional sensitivity analysis using two and four modes for active shot data 2021.08.12. (A-C) Shear-wave velocity for layers 1-3 using two modes. (D-F) Shear-wave velocity for layers 1-3 using four modes. (G-I) Thickness for layers 1-3 using two modes. (J-L) Thickness for layers 1-3 using four modes. The mismatch gives the normalized difference between observed and predicted data given as values between 0 and 1.

637x511mm (177 x 177 DPI)

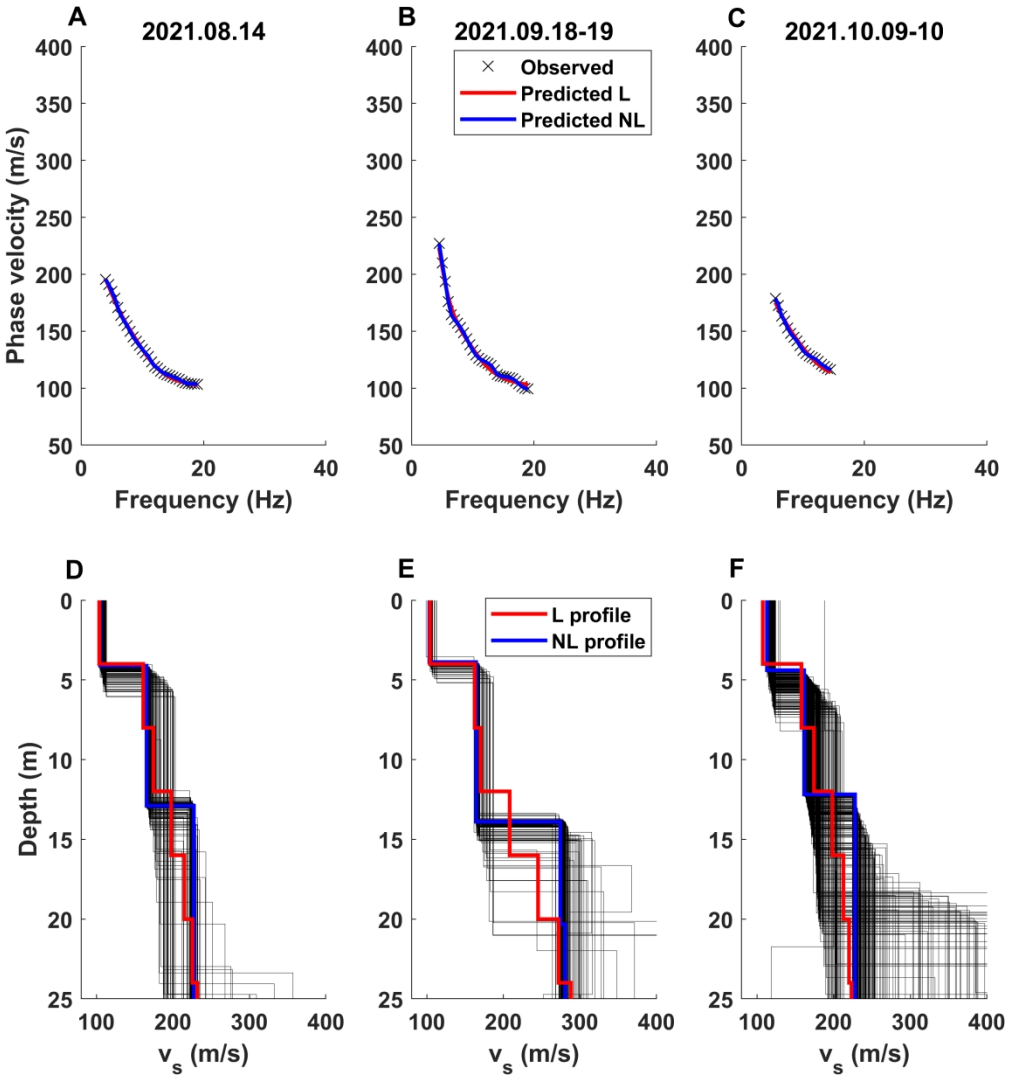

Figure 8: Same as Figure 6 but for the inversion of one mode obtained from the ambient noise interferometry.

479x511mm (177 x 177 DPI)

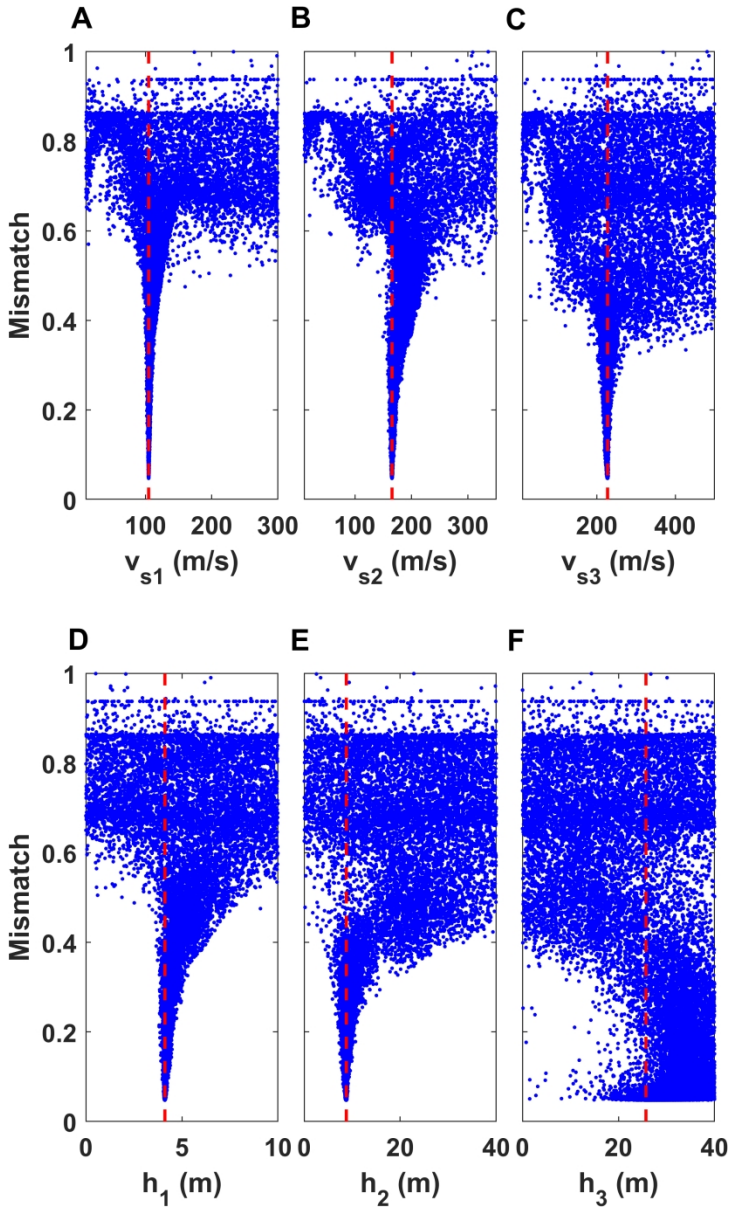

Figure 9: Multidimensional sensitivity analysis for ambient noise data on 2021.08.14. (A-C) Shearwave velocity for layers 1-3. (D-F) Thickness for layers 1-3.

307x512mm (177 x 177 DPI)

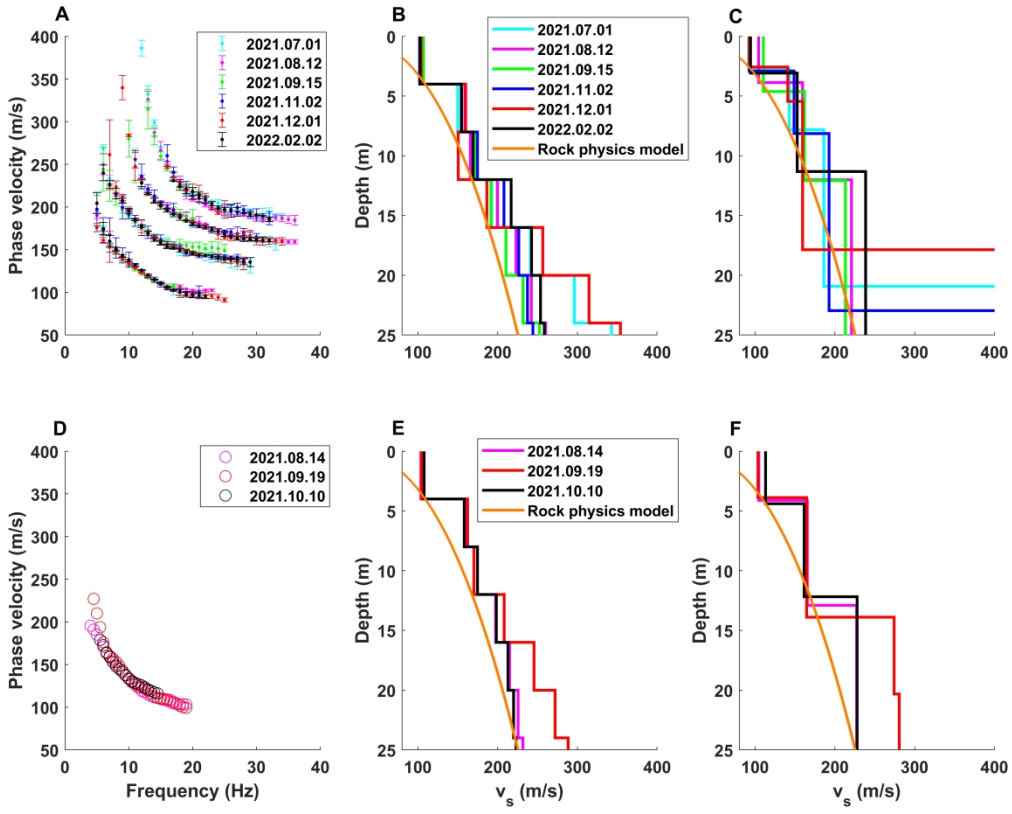

Figure 10: Dispersion curves and inversion results from active shots (A-C) and ambient noise interferometry (D-F). (A) The mean dispersion curves from the different shot days with error bars indicate one standard deviation. (B) The linearized inversion profiles using two modes. (C) The ASSA inversion profiles using two modes. (D) Dispersion curves from the interferometry. (E-F) The linearized and ASSA inversion profiles, respectively. (B, C, E, F) are all overlaid with the predicted vs profile from the rock physics modeling (see Appendix C for more details).

639x511mm (177 x 177 DPI)

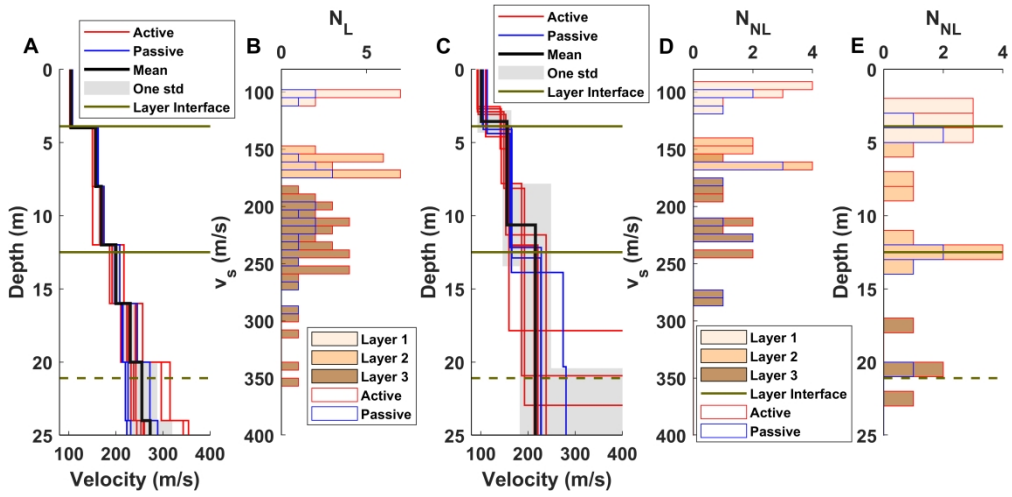

Figure 11: Time-lapse analysis of the inversion profiles for the active and passive data over the seven-month acquisition period. (A) Velocity profiles obtained from the linearized inversion for the active (red) and passive data (blue) with mean profile (black) and one standard deviation (std) over velocity profiles found using active and passive data, indicating the variation over the acquisition period (gray shaded area). Note that the time-lapse of shear-wave velocity profiles have not been separated by color (see Figure 10). (B) Associated velocity distribution with N_L velocity values from the linearized inversion, color-coded by the interpreted layers. (C) and (D) are the same as (A) and (B) but from ASSA inversion with N_NL velocity values. (E) Associated depth distribution with N_NL depth values from the non-linear inversion. The layers are interpreted from (E), indicated as solid lines for the layers within the resolution rule of thumb, and dashed when outside. For an overview of the individual estimated values from the active and passive data, see Table 4.

591x288mm (177 x 177 DPI)

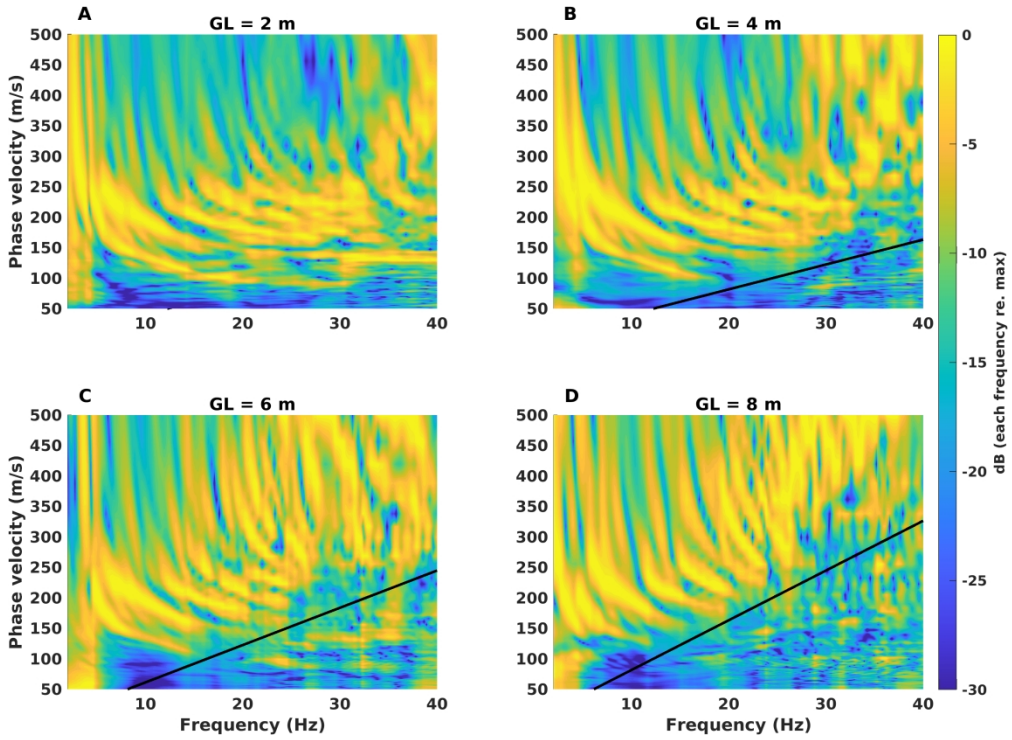

Figure A-1: Comparison of dispersion images from data using different gauge lengths (GL). The black line is computed as the case when the wavelength is equal to GL, i.e., f = v_{phase}/GL.

695x507mm (118 x 118 DPI)

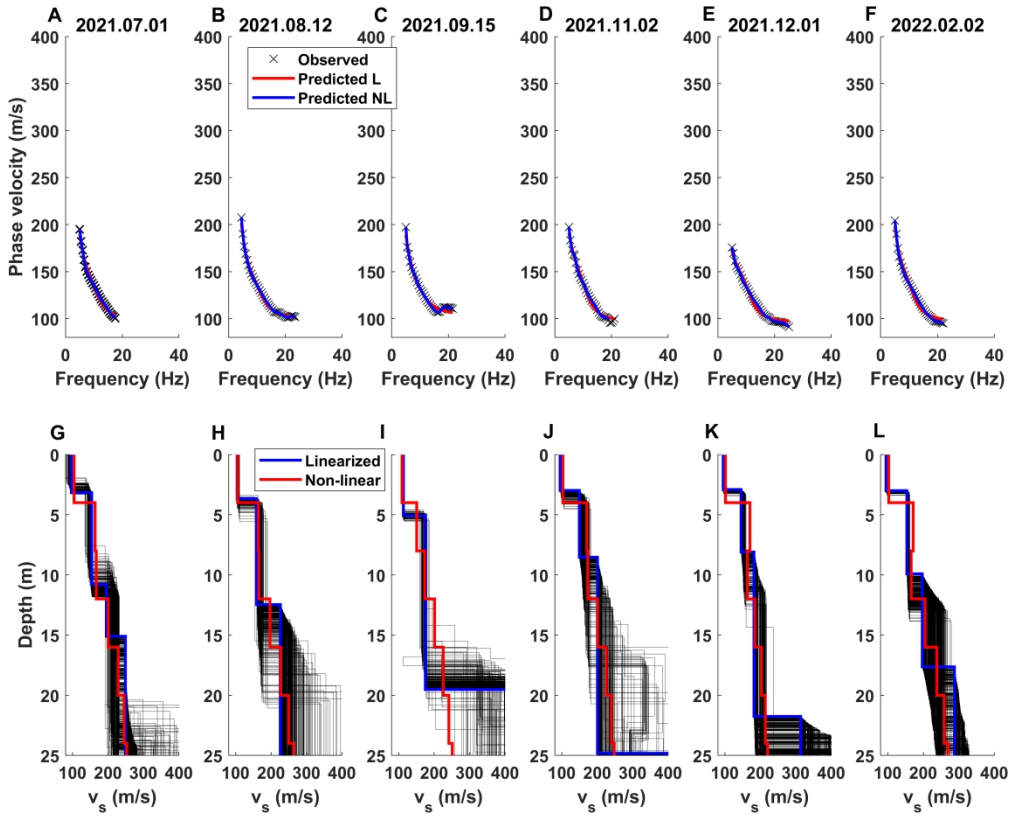

Figure B-1: Observed and predicted dispersion curves for one mode from active data and the associated inversion results. (A-F) The fit between the observed (black) and the predicted (red for linearized, blue for ASSA) dispersion curves. (G-L) The estimated shear-wave velocity profiles from the linearized (L; red) and ASSA non-linear (NL; blue) inversion overlay a subset of the velocity profiles (black) generated by the ASSA inversion. The ensemble illustrated the uncertainty of the parameter estimation.

633x511mm (177 x 177 DPI)

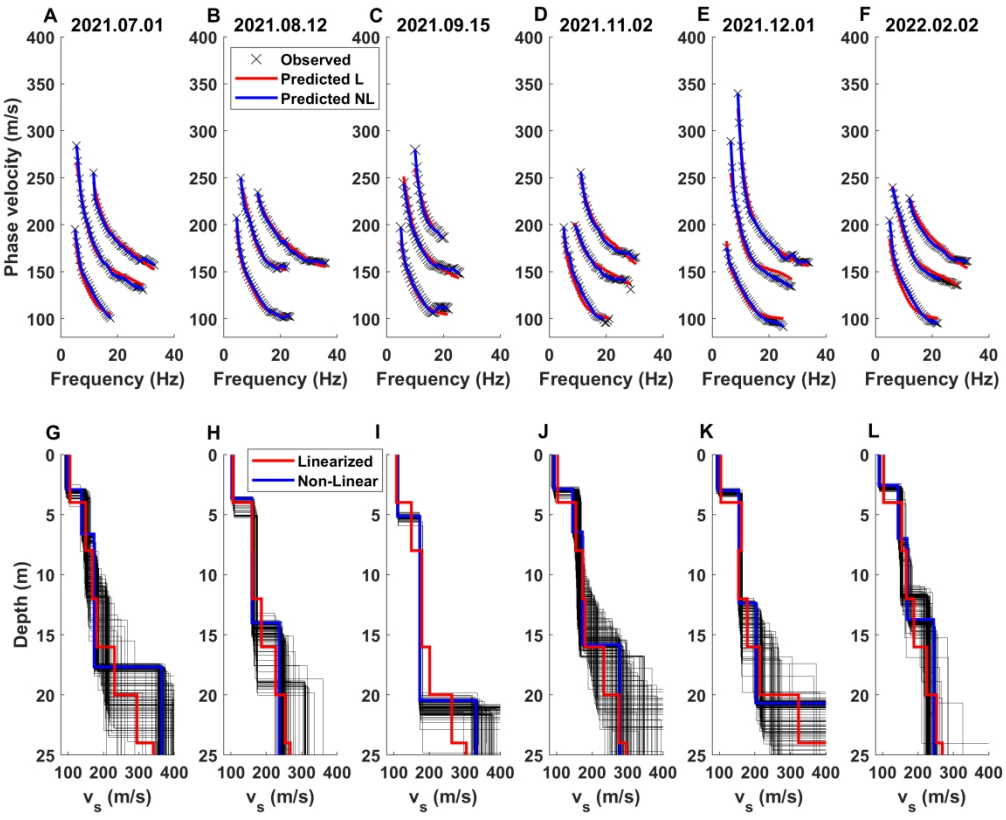

Figure B-2: Same as Figure 6 and Figure B-1 but for the inversion of three modes.

634x512mm (118 x 118 DPI)

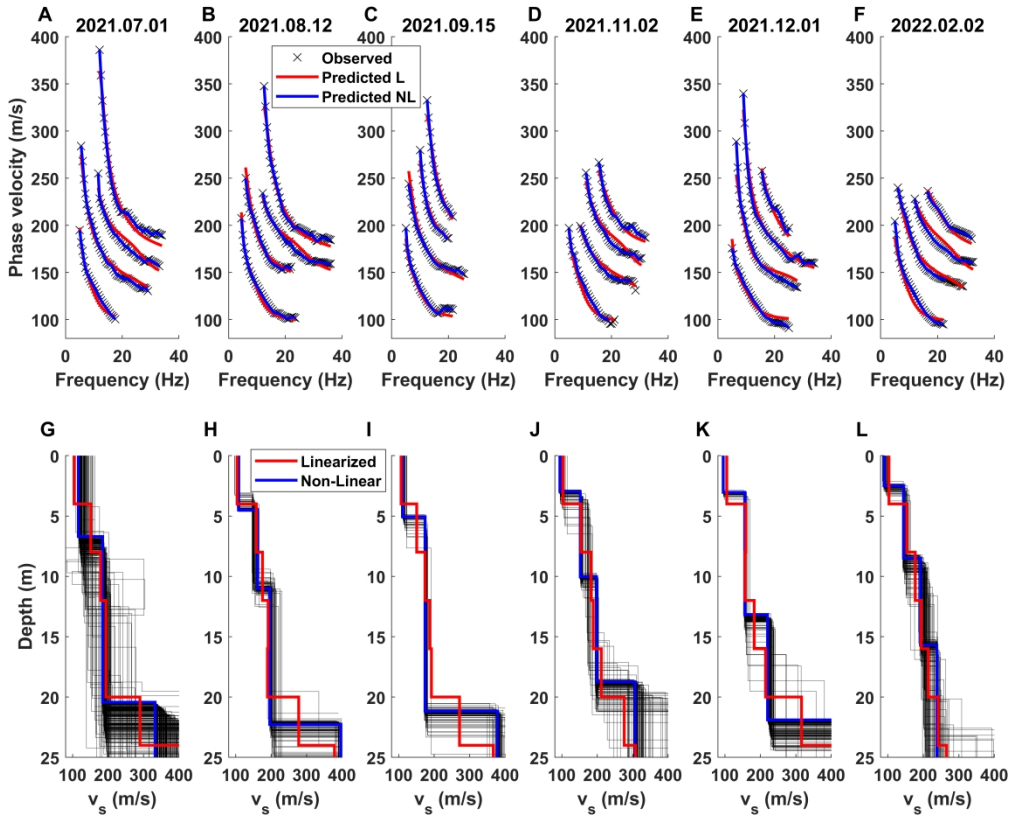

Figure B-3: Same as Figure 6 and Figure B-1 but for the inversion of four modes.

633x512mm (177 x 177 DPI)

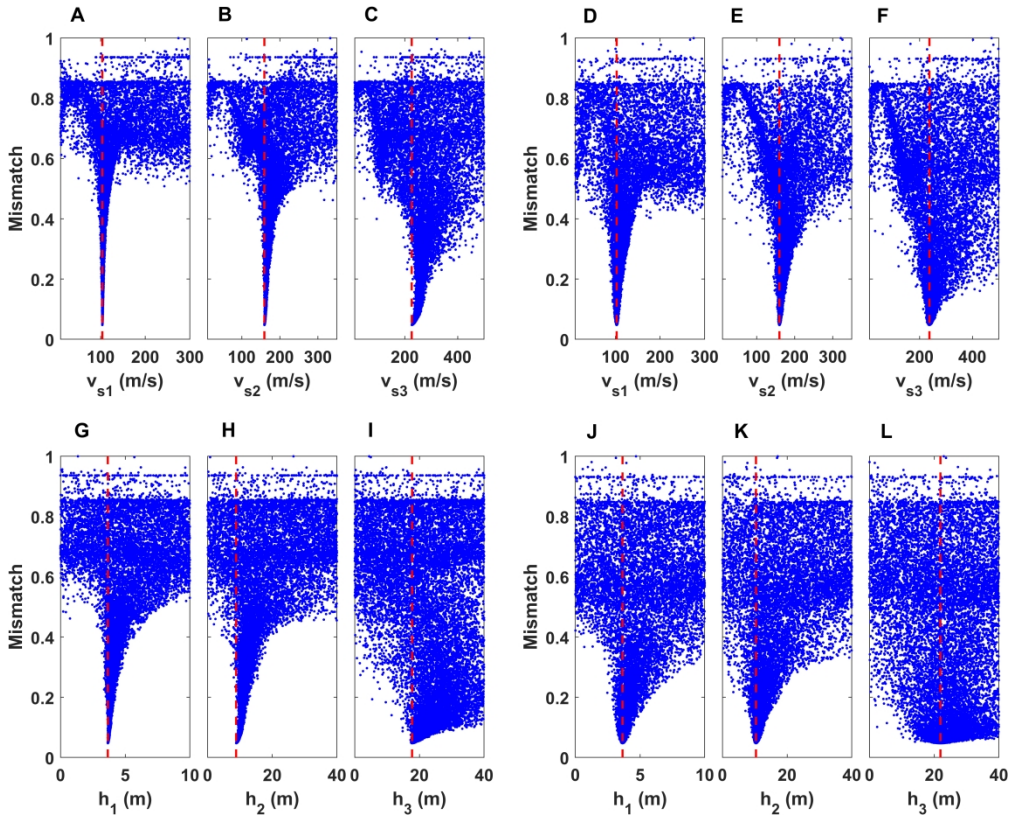

Figure B-4: MDS from 2021.08.12 for one mode (A-C and G-I) and three modes (D-F and J-L).

634x513mm (177 x 177 DPI)

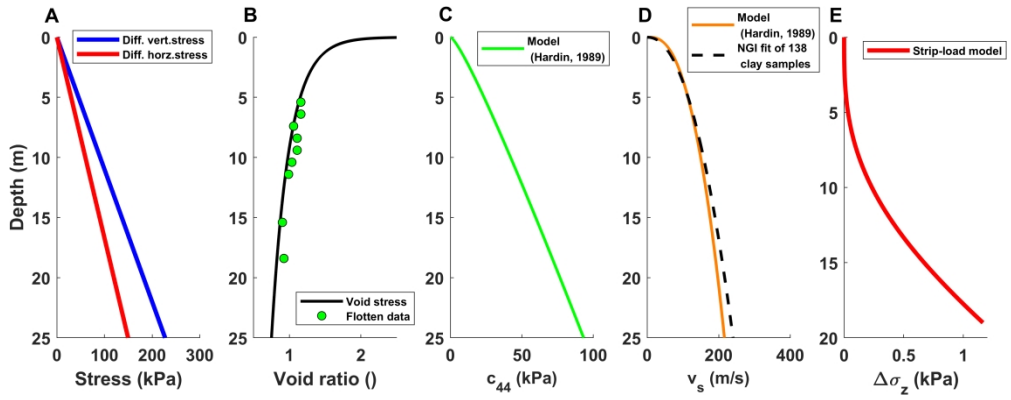

Figure C-1: Stress (A) and void ratio (B) depth profiles as a function of depth are used in estimating the shear modulus depth trend at the Rissa acquisition site when assuming hydrostatic pore pressure conditions. In (B), the green dots represent the average bulk density estimated from lab analysis of quick clay samples of the Tiller site in Trondheim, Norway. (C) The predicted shear modulus depth profile using the model of equation C-1. (D) The corresponding synthetic shear wave velocity depth profile (orange) along with NGI's fitted regression line is based on 138 clay cores (black) acquired from central- and eastern-Norway (L'Heureux et al., 2015). (E) The vertical stress change as a function of depth is estimated using the strip-load model (Boussinesq, 1885).

633x246mm (177 x 177 DPI)